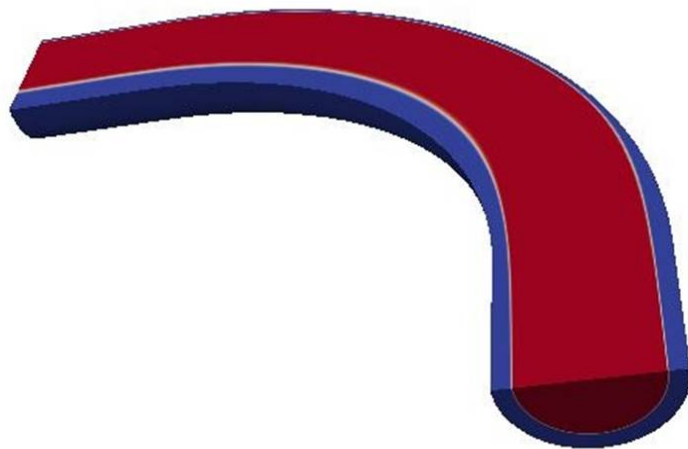


Numerical Simulation of Core-Annular Flow in a Curved Pipe

Simulation of two phase flow with OpenFOAM
Report Number:2625(MEAH:277)

S. M. Park

Master of Science Thesis



Numerical Simulation of Core-Annular Flow in a Curved Pipe

Simulation of two phase flow with OpenFOAM

Report Number:2625(MEAH:277)

MASTER OF SCIENCE THESIS

For the degree of Master of Science in Sustainable Process and Energy
Technology at Delft University of Technology

S. M. Park

June 24, 2014

Faculty of Mechanical, Maritime and Materials Engineering (3mE) · Delft University of
Technology



Abstract

A numerical study, using the volume-of-fluid method (VOF), has been made of core-annular flow in a curved pipe. We investigated two cases: core-annular flow in a 90° bend and in a 180° return bend. To verify our numerical method we first compared our results for a single-phase flow in a 90° bend with numerical results and experimental data given in the literature. The agreement was good. Thereafter a detailed analysis has been made for the velocities and pressures occurring in a 90° bend and in a 180° return bend. Special attention was given to the influence of secondary flows perpendicular to the pipe axis. These secondary flows play an important role in the behaviour of core-annular flow in a curved pipe.

Table of Contents

Acknowledgements	v
1 Introduction	1
2 Multiphase Flow	5
2-1 Introduction	5
2-2 Flow pattern	5
2-3 Dimensionless numbers	7
3 Perfect Core Annular Flow	9
3-1 Introduction	9
3-2 Velocity distributions	9
4 Numerical method	13
4-1 Introduction	13
4-2 Spatial discretization	13
4-3 Time step restrictions	14
4-4 Volume-of-Fluid Method	14
4-5 Geometry	15
4-6 Boundary conditions and initial conditions	16
5 Single-Phase Flow in a 90° Bend	17
5-1 Introduction	17
5-2 Basic equations	18
5-3 Boundary conditions	19
5-4 Single Phase flow in 90° bend	20
5-4-1 Axial velocity distribution	20
5-4-2 Contour plots for axial velocity distribution	21
5-4-3 Secondary flow velocity	22
5-4-4 Conclusion	23

6	Core-Annular Flow in a 90° bend	29
6-1	Geometry and boundary condition	30
6-2	Core-annular flow in a 90° bend without buoyancy effect	30
6-2-1	Core shape and position in the pipe	30
6-2-2	Axial and secondary flows	33
6-2-3	Pressure distribution	35
6-3	Core-annular flow in a 90° bend with buoyancy effect	36
6-3-1	Core shape and position in the pipe	36
6-3-2	Axial and secondary flows	37
6-3-3	Reduced pressure	39
6-4	Conclusion	40
7	Core-annular flow in 180° return bend	43
7-1	Introduction	43
7-2	Geometry and boundary condition	44
7-3	Parameter values	44
7-4	Results	46
7-4-1	Core shape and position in the pipe	46
7-4-2	Secondary flows	50
7-4-3	Axial velocity	50
7-4-4	Pressure distribution	53
7-5	Conclusion	54
8	Recommendations	57

Acknowledgements

I would like to express my deep appreciation to prof.dr.ir. G.Ooms and dr.ir. M.J.B.M.Pourquie, my research supervisors, for their patient guidance, useful advice and warm encouragement for my research work. I would also like to thank dr.ir. G.H.Keetels for participating in my graduation committee and for his time devoted to reading my thesis.

I really appreciate my family in South Korea for their support and encouragement to finish my study in the Netherlands.

Delft, University of Technology
June 24, 2014

S. M. Park

Chapter 1

Introduction

In recent decades the amount of energy consumption has increased enormously. As a consequence the usage of natural resources has dramatically increased and their depletion has become a serious problem. Especially the depletion of light oils (low-viscosity oils) is seriously influencing the world economy. To solve this problem one looks for a substitute resource to replace the light oils. A possibility is to use heavy oils (high-viscosity oils). Due to the high viscosity of this oil a large pumping power is required to transport it. A possibility to reduce the pressure drop is to use water to lubricate the oil.

There are several types of flow patterns for oil-water transport through a pipeline. When the gravity effect is strong a stratified flow is present, where the lighter liquid (usually oil) is on top of the heavier liquid. In that case only a part of the pipe wall is in contact with the water. A more promising flow pattern (from a pressure gradient point of view) is oil-water core-annular flow. In that case the oil core is completely surrounded by a thin layer of water that acts as a lubricating film, thus reducing the pressure drop very considerably.

The earliest study about the application of core-annular flow was by Issacs and Speed (1904). They generated core-annular flow by using a riffle inside the pipe wall. Due to the centrifugal force (caused by the riffle) the water was pushed to the wall, thus generating a core-annular flow. Due to the buoyancy force on the oil core (caused by the density difference between oil and water) the core had the tendency to drift upwards and foul the upper part of the pipe wall. However when the centrifugal force due to the riffle was large enough, there remained a water layer between the oil core and the pipe wall.

The first laboratory test of core-annulus flow was carried out by Clark (1948). He found that when the density difference of the two liquids is small and the viscosity difference large enough, the low-viscosity liquid encapsulates the high-viscosity one. Clark carried out tests with heavy crude oil and water. Clark and Shapiro (1949) removed the buoyancy effect by matching the density of the heavy oil with the water density by adding a substance to the oil. Ooms et al.[1] showed that hydrodynamic forces are exerted on the oil core due to the water flow in the annular layer, which counterbalance the buoyancy force on the core. It was

assumed that such forces were due to the movement of waves at the oil-water interface with respect to the tube wall.

Generally the studies about core-annular flow have focused on straight vertical or horizontal pipes. There are not many studies on core-annular flow in a curved pipe. However during pipeline transport of heavy oil one has to deal with curved parts in the pipe. Compared to core-annular flow in a straight pipe such a flow in a curved pipe is considerably more complicated. The centrifugal force has a strong influence on the flow pattern, causing secondary flows perpendicular to the pipe axis. Fouling is likely to occur easier than for a straight pipe. Therefore we decided to study core-annular flow in a curved pipe in more detail.

The flow in a curved pipe is three dimensional. First we analyzed single phase flow in a curved pipe flow to investigate the curvature effect on such a flow. A 90° bend was chosen as model geometry with a curvature ratio of $1/6$. We concentrated in particular on the shift in the location of maximum axial velocity and on the secondary velocity components caused by the centrifugal forces.

Thereafter we extended the study to core-annular flow in a 90° bend. We used the same flow properties as applied by Ooms et al.[6] for a straight pipe. In the first calculation we neglected the buoyancy effect to study in particular the effect of the centrifugal force on core-annular flow in a bend. Thereafter we implemented the buoyancy effect to analyse the simultaneous effect of both buoyancy and centrifugal force on core-annular flow in a bend. The same curvature ratio as used for the single phase flow was applied. We studied in detail the deformation of the core-annular interface, the axial velocity distribution, the secondary flow development and the pressure distribution. In our curved core-annular flow study we did not start with a wavy core-annular interface and the pipe length was too small to see the development of such a wave.

After completing the study regarding the 90° bend we extended our study to a 180° return bend as the last part of our study. We carried out this calculation as experimental results on such a flow geometry were available in the open literature by Sharma et al.[9]. They studied up-, down- and horizontal flow of the 180° return bend for a range of oil and water superficial velocities. Information was given by them, for instance, about the flow pattern and pressure drop. We selected a case from their study in the horizontal core-annular flow regime and compared our result for the pressure gradient with their result.

For our study we used CFD (computational fluid dynamics). The capacity for fluid-flow calculations has dramatically increased in recent decades, thereby making numerical analysis of complicated flows (like core-annular flow) is possible. A range of commercial codes is available nowadays, but their use is still expensive. However rather recently also open-source codes have been developed, that are freely available. We have applied the OpenFoam code. We used the OpenFoam version 2.1.1 package as our CFD code to investigate numerically core-annular flow in a curved pipe. There exist many types of different solvers in OpenFoam and we applied the multiphase solver using the VOF (volume of fluid) method which is called 'interFoam'.

The main purpose of this thesis is to understand the physical phenomena of core-annular

flow in a curved pipe. In chapter 2 and chapter 3 we present the theory of multiphase flow related to core-annular flow and PCAF (Perfect Core-Annular Flow), respectively. In chapter 4, single phase flow in the 90° bend is treated and we analyze in particular the secondary velocity components and their influence on the flow development. In this chapter our computation results are compared with FEM-calculations and experimental results given in the literature. In chapter 5 core-annular flow in the 90° bend is treated. Two different simulations have been carried out in this chapter to see the separate effects of the centrifugal force and buoyancy force. In chapter 6 our study regarding core-annular flow in a return bend pipe is presented. The flow properties in the different parts of the pipe are discussed.

Chapter 2

Multiphase Flow

2-1 Introduction

Practical applications of fluid dynamics are often concerned with multiphase flows. In particular, the flow of two immiscible liquids occurs in a range of processes and equipments in, for instance, the petroleum industry. In our study we limit ourselves to the two-phase flow of oil and water through a pipeline. Accurate knowledge of the flow properties (such as flow pattern, water hold-up and pressure gradient) is essential. Different flow patterns are possible: oil drops in water, oil slugs in water, stratified flow and core-annular flow. Because of these various types of flow patterns the study of two-phase flow is more complicated than of single-phase flow. In order to understand two-phase flows a knowledge of the relevant dimensionless parameters is helpful. For two-phase flows more dimensionless parameters exist than for single-phase flow. In this chapter the dimensionless parameters of two-phase flows are presented and discussed.

2-2 Flow pattern

In figure 2-2 the various types of multiphase flow patterns are presented: stratified flow, bubbly flow, slug flow, dispersed flow and core-annular flow. In stratified flow there is a complete separation of oil and water. This flow pattern can be formed in a limited range of relatively low flow rates where the stabilizing gravity force due to a density difference between the two liquids is dominant. By increasing the water flow rate the oil core breaks up in large slugs or drops. The oil drops are generated due to capillary instabilities in the presence of shear. If the water flow rate is sufficiently large, the entire oil phase breaks up into small droplets which results in an oil-in-water dispersion. If the dispersion is very stable, the flow is called an emulsion.

In core-annular flow the oil core is completely surrounded by a layer of water, which acts

as a lubricating film. It is the most attractive flow pattern from a pressure drop reduction point of view and therefore of interest for the pipeline transport of heavy (high-viscosity) oil. Dependent on the location of the core centerline the flow pattern can be sub-divided in a number of patterns: fully eccentric, eccentric and concentric core flow (see figure 2-1). Which flow pattern occurs depends on a number of parameters, such as the density difference between the oil and water, the superficial velocities of the liquids and the pipe diameter. Concentric core-annular flow with a smooth oil-water interface is called perfect core-annular flow (PCAF). The flow equations for a smooth core-annular flow (concentric and eccentric) have been solved analytically. For the other flow patterns numerical calculations are needed.

PCAF can be considered the ideal flow pattern of core-annular flow. However, due to the interaction between the two liquids PCAF does not often occur. Joseph et al [2] analysed experimentally the various core-annular flow patterns in a horizontal pipe as a function of the superficial velocities of oil and water (see figure 2-2).

As mentioned we will concentrate on core-annular flow in a horizontal curved pipe. For a straight pipe theoretical models have been developed to understand the levitation force on the core, which counterbalances the buoyancy force. In these models the presence of waves at the interface is crucial. In this work we will not pay attention to this aspect of core-annular flow.

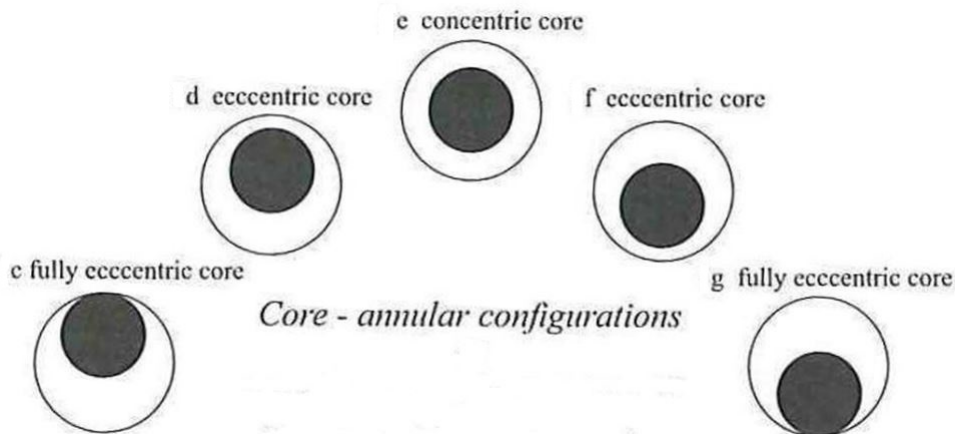


Figure 2-1: The flow patterns of core-annular flow classified according to the centerline position of the core [11]

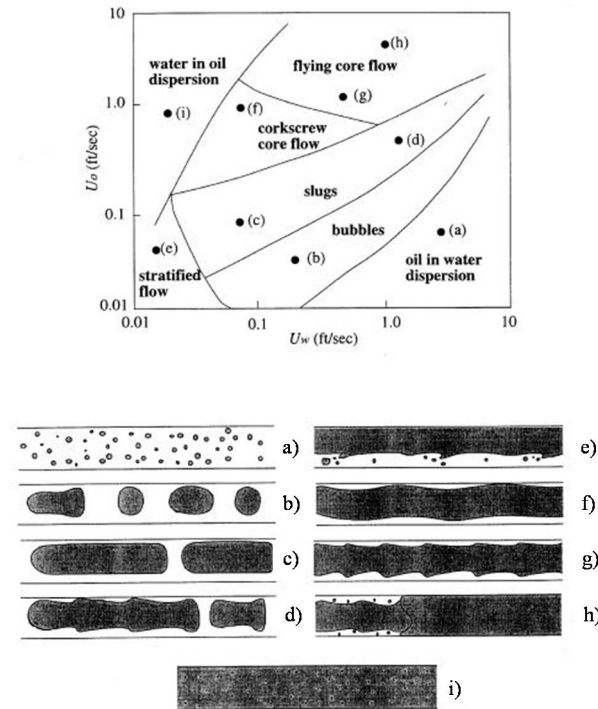


Figure 2-2: The various flow patterns of core-annular flow in a horizontal pipe as a function of the superficial velocities [2]

2-3 Dimensionless numbers

In a multiphase flow five different forces play a role. With a characteristic length L and characteristic velocity U the forces are given by:

- inertial force $\rho U^2 L^2$
- pressure force $\Delta P L^2$
- gravity force $\rho g L^3$
- viscous force $\mu U L$
- surface tension force σL

A dimensionless number is found by the ratio of two of these forces. Some familiar examples are given below:

Reynolds number:

$$Re = \frac{L\rho U}{\mu} \quad (2-1)$$

Froude number:

$$Fr = \frac{U^2}{gL} \quad (2-2)$$

Weber number:

$$We = \frac{L\rho U^2}{\sigma} \quad (2-3)$$

For the specific problem of core-annular flow six dimensionless groups are relevant. These dimensionless numbers are listed below. The indices o and w indicate the properties of oil and water respectively.

Viscosity ratio:

$$m = \frac{\mu_w}{\mu_o} \quad (2-4)$$

Ratio of pipe radius and undisturbed oil radius:

$$a = \frac{R_2}{R_1} \quad (2-5)$$

Density ratio:

$$\zeta = \frac{\rho_w}{\rho_o} \quad (2-6)$$

Ratio of driving forces in core and annulus:

$$K = \frac{(f^* + \rho_o g)}{(f^* + \rho_w g)} \quad (2-7)$$

Where f^* is the driving pressure gradient.

Surface tension parameter:

$$J = \frac{\sigma^* R_1 \rho_o}{\mu_o^2} \quad (2-8)$$

where σ^* is the surface tension at the interface of the two liquids.

Reynolds number for oil and water:

$$Re_i = \frac{\rho_i V_0^*(0) R_1}{\mu_i} \quad (2-9)$$

where $V_0^*(0)$ is the centerline velocity for perfect core-annular flow and $i = o, w$

Perfect Core Annular Flow

3-1 Introduction

PCAF is the ideal flow pattern among the various core-annular flow patterns. In this thesis we implemented PCAF to set up the initial condition inside the pipe and boundary condition at the pipe inlet of core-annular flow in a curved pipe. To that purpose we used the velocity profile for PCAF derived by Li and Renardy [4]. In this chapter the relevant analytical expressions for PCAF are given.

3-2 Velocity distributions

For the derivation of the velocity profile of PCAF Li and Renardy used the equation of motion for an incompressible flow in cylindrical coordinates given by equation 3-1 to 3-3. Later on when we discuss the flow in a curved pipe, a different version of the equation of motion is used.

$$\rho \left(\frac{\partial u}{\partial t} + u \frac{\partial u}{\partial r} + v \frac{\partial u}{\partial x} \right) = -\frac{\partial P}{\partial r} + \frac{1}{r} \frac{\partial (r S_{rr})}{\partial r} + \frac{\partial S_{xr}}{\partial x} - \frac{S_{\theta\theta}}{r} + F_r \quad (3-1)$$

$$\rho \left(\frac{\partial v}{\partial t} + u \frac{\partial v}{\partial r} + v \frac{\partial v}{\partial x} \right) = -\frac{\partial P}{\partial x} + \frac{1}{r} \frac{\partial (r S_{rx})}{\partial r} + \frac{\partial S_{xx}}{\partial x} + \rho g + F_x \quad (3-2)$$

$$\nabla \cdot u = \frac{1}{r} \frac{\partial ru}{\partial r} + \frac{\partial v}{\partial x} = 0 \quad (3-3)$$

where $S_{rr} = 2\mu(\partial u/\partial r)$, $S_{\theta\theta} = 2\mu(u/r)$, $S_{xx} = 2\mu(\partial v/\partial x)$, $S_{xr} = S_{rx} = \mu(\partial v/\partial r + \partial u/\partial x)$. The radial and axial components of the velocity are denoted by u and v respectively. F_r and F_x are body forces which include the interfacial tension in the VOF formulation.

Starting from these equations Li and Renardy[1999] derived the following expressions for the dimensionless velocity in the core and annulus.

Annulus:

$$V(r) = \left[a^2 - r^2 - 2(K-1)\log\left(\frac{r}{a}\right) \right] / A \quad (3-4)$$

Core:

$$V(r) = 1 - mr^2K/A \quad (3-5)$$

$$A = mK + a^2 - 1 + 2(K-1)\log a \quad (3-6)$$

r has now been made dimensionless by means of R_1 . The velocities have been made dimensionless by the centerline velocity $V_0^*(0)$, given by

$$V_0^*(0) = (f^* + \rho_2g) \frac{R_1^2}{4\mu_2} A. \quad (3-7)$$

Hold-up ratio

The dimensionless flow rates can be calculated by integrating these velocity fields

$$\begin{aligned} Q_o &= 2\pi \int_0^1 rV(r) dr \\ &= 2\pi \int_0^1 \left(r - mr^3K/A \right) dr \\ &= 2\pi \left[\frac{1}{2}r^2 - \frac{mK}{4A}r^4 \right]_0^1 \\ &= \pi \left(1 - \frac{mK}{2A} \right) \end{aligned} \quad (3-8)$$

and

$$\begin{aligned} Q_w &= 2\pi \int_1^a rV(r) dr \\ &= \frac{2\pi}{A} \int_1^a \left(a^2r - r^3 - 2(K-1)r\ln(r) + 2r(K-1)\ln(a) \right) dr \\ &= \frac{2\pi}{A} \left[\frac{1}{2}a^2r^2 - \frac{1}{4}r^4 - (K-1) \left(r^2\ln(r) - \frac{1}{2}r^2 \right) + r^2(K-1)\ln(a) \right]_1^a \\ &= \frac{\pi}{A} \left(\frac{1}{2}a^4 + (K-2)a^2 + \frac{1}{2} - (K-1)(1 + 2\ln(a)) \right). \end{aligned} \quad (3-9)$$

The dimensional flow rates can be obtained from

$$Q_o^* = Q_o V_0^*(0) R_1^2 \quad (3-10)$$

and

$$Q_w^* = Q_w V_0^*(0) R_1^2. \quad (3-11)$$

From these flow rates the superficial velocities can be calculated as,

$$u_{o,s}^* = \frac{Q_o^*}{\pi R_2^2} \quad (3-12)$$

and

$$u_{w,s}^* = \frac{Q_w^*}{\pi R_2^2}. \quad (3-13)$$

According to its definition the hold-up is then equal to

$$h = \frac{Q_o H_w}{Q_w H_o} = \frac{(a^2 - 1) Q_o}{Q_w}. \quad (3-14)$$

in which H_o and H_w are the volume fractions of oil and water.

Numerical method

4-1 Introduction

For our numerical analysis the package OpenFoam version 2.1.1 is applied. In order to simulate two fluids of different densities the volume-of-fluid (VOF) method is an important numerical method. We applied the interFoam solver in the package OpenFOAM which uses the VOF method. OpenFoam uses the finite volume method (FVM) for representing the relevant partial differential equation in the form of algebraic equations. Selecting the proper numerical schemes is essential to solve the flow problem correctly. In this chapter the important numerical schemes, time step restriction and VOF method that we used are explained.

4-2 Spatial discretization

In the system directory of OpenFoam (fvSchemes dictionary) the relevant numerical schemes for each term of the equations can be selected. For the time term we used the backward Euler method (implicit method).

$$\frac{dy}{dt} = f(t, y) \quad (4-1)$$

$$y_{k+1} = y_k + hf(t_{k+1}, y_{k+1}) \quad (4-2)$$

The Gauss limited linear V method is used for the advection terms of the velocity component and the Gauss van Leer for the advection term of the scalar.

For the pressure-velocity coupling the PIMPLE scheme is applied. In the OpenFoam version 1.6 the PISO (pressure implicit with splitting of operators) scheme was used for the

pressure-velocity coupling. However it cannot be used in OpenFoam version 2.1.1. PIMPLE is the merged PISO-SIMPLE (semi-implicit method for pressure linked equations) scheme. It is used for large time-step transient incompressible flows. The following linear solvers are used: Preconditioned Conjugate Gradient for the pressure (tolerance is 10^{-10}), and Preconditioned Bi-Conjugate Gradient for velocity components (tolerance is 10^{-7}).[21]

4-3 Time step restrictions

The Courant-Friedrichs-Lewy (CFL) is an important condition to ensure convergence. The interFoam solver uses an adjustable time step based on the maximum Courant number in the domain. J.C. Beerens [12] tested various Courant numbers for stability reason in his study and he found that the Courant number needs to be as small as 0.02 to obtain accurate solution for core-annular flow. For our study we used the same Courant number. The Courant number is defined by the equation 4-3.

$$Co = \Delta t \sum_{i=1}^n \frac{u_i}{\Delta x_i} \quad (4-3)$$

Besides the Courant number the surface tension also influences the stability of the solver. The surface tension plays a vital role in multiphase flows and it will impose a restriction on the time step. The exact restriction imposed by the surface tension on the time step is given by equation 4-4. [12]

$$\Delta t \leq \max(10\tau_\mu, 0.1\tau_p) \quad \text{with} \quad \tau_\mu = \frac{\mu\Delta x}{\sigma} \quad \text{and} \quad \tau_p = \sqrt{\frac{\rho\Delta x^3}{\sigma}} \quad (4-4)$$

4-4 Volume-of-Fluid Method

In a VOF method an indicator function is used to determine the fraction of one of the fluids in a cell. This indicator function, α_1 is equal to 1 when the cell is completely filled with the primary fluid, and equal to 0 when the cell is filled with the secondary fluid. Also intermediate values can occur. Actual values of density and viscosity are calculated using this indicator function for every cell via equation 4-5 and 4-6 respectively. The transport of this indicator function is done with the advection equation 4-7. Combining these equations with the Navier-Stokes equations (4-8) and mass conservation equation (4-9) gives the set of equations which has to be solved.[3]

$$\rho = \alpha_1\rho_1 + (1 - \alpha_1)\rho_2 \quad (4-5)$$

$$\mu = \alpha_1\mu_1 + (1 - \alpha_1)\mu_2 \quad (4-6)$$

$$\frac{\partial \alpha_1}{\partial t} + \nabla \cdot (\mathbf{u} \alpha_1) = 0 \quad (4-7)$$

$$\frac{\partial u_i}{\partial t} + u_j \frac{\partial u_i}{\partial x_j} = -\frac{1}{\rho} \frac{\partial p}{\partial x_i} + \nu \frac{\partial^2 u_i}{\partial x_j^2} + g_i \quad (4-8)$$

$$\frac{\partial u_i}{\partial x_i} = 0 \quad (4-9)$$

Solving this system is not straightforward. Preserving the sharpness of the interface is also very important for a volume-of-fluid method. In interFoam in contradiction to other state-of-art codes no geometric reconstruction is made. The algorithm employs a compressive-flux model called 'interfaceCompression', which limits the diffusion of the indicator function. [19]

4-5 Geometry

We studied two different cases for the computation domain: the 90° and 180° bend flow. For the 90° bend we studied single and core-annular flow and for the 180° return bend only core-annular flow. The curved flow does, of course, not fulfill the condition of axi-symmetry, so a three-dimensional flow is present.

J. C. Beerens evaluated the performance of different numbers of grid points in his master thesis. He tested three different meshes, 64 × 64, 128 × 128, and 256 × 256, and different time steps. He found that 128 × 128 grid cells is required with $Co = 0.02$ to achieve the same results for the growth rate as found from linear stability theory for axisymmetric flows. [12].

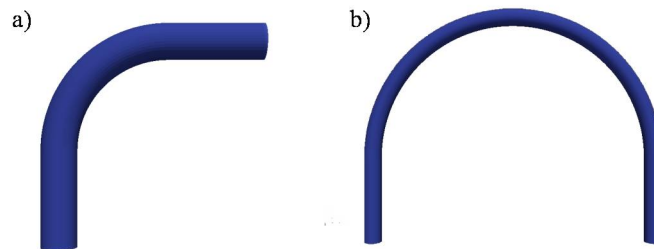


Figure 4-1: Computation domain, a) 90° curved bend, b) 180° curved bend

Our calculations for a curved pipe are not axisymmetric, but are three-dimensional. So we could not afford the same number of grid cells in radial direction as applied by Beerens because of computation time. In the axial flow direction of the pipe we used an equidistant, orthogonal and non-stretched grid. In case of a core-annular flow we applied in the radial direction a structured mesh for the annulus and core. For the single-phase calculations we

used 40, 40, and 80 grid cells in radial, circumferential, and axial flow direction, respectively. For the core-annular flow in the 90° bend 114, 88, and 91 grid cells were applied in radial, circumferential, and axial flow direction. (For the radial direction we used 44 structured grid cells in the annulus and 48 structured grid cells for the core with double side aspect ratio of 15%. At the center of the core 22 structured grid cells were used). For the core-annular flow in the 180° return bend we used 86, 80, and 103 grid cells in radial, circumferential, and axial flow direction. (For the radial direction we used 36 and 30 structured grid cells in annulus and core, respectively. The aspect ratio was 7% at the wall side and 5% at the center. At the center of the core 22 structured grid cells were used). Due to the movement of the core towards the pipe wall we implemented more closely packed grid cells near the wall than in the core region.

4-6 Boundary conditions and initial conditions

The boundary conditions for the domain are as follows. On the pipe wall a no-slip boundary condition was imposed. On the inflow cross section of the pipe the groovy boundary condition was imposed for the core-annular inlet velocity profile and zero velocity gradient at the outlet. At the outlet a fixed value was imposed for the reduced pressure. A back-flow occurred for a zero-gradient condition. The initial velocity distribution was set equal to the analytical solution of Li and Renardy for perfect core-annular flow. No initial wave at the core-annular interface was applied. In our study we did not pay attention to the possible wave development at the interface.

Single-Phase Flow in a 90° Bend

5-1 Introduction

Compared to the flow in a vertical or horizontal straight pipe the physical phenomena of the flow in the curved pipe are significantly different. The curved-pipe flow is influenced by gravity and centrifugal force while a straight-pipe flow is only influenced by gravity effects. Due to the centrifugal force a secondary flow motion develops when the liquid flows through the curved area of the pipe. The study of curved-pipe flow is quite important for all kind of applications, such as flow in a heat exchanger, oil transport through a pipe, blood flow through a vessel, etc. The purpose of our study is to investigate the influence of a pipe curvature on core-annular flow. In this chapter single-phase curved pipe flow is studied. In the next chapters core-annular flow in a curved pipe is investigated.

In order to make a balance between the pressure gradient and the centrifugal forces, the slow liquid particles should pass through the inner-curve part of the curved pipe, while the fast liquid passes through the outer-curve part. This causes the development of secondary flows perpendicular to the pipe axis in the curved pipe region. At the center line of the pipe cross section the secondary velocity flows from the inner to the outer curve, and returns back from the outer curve to the inner one along the pipe wall. In this way two vortices develop in the plane of the pipe cross section. These vortices push the maximum axial velocity toward to the outer curve of the pipe.

To study curved tube flow two dimensionless parameters are quite important: the curvature ratio (δ) and Dean number (κ). By implementing a toroidal coordinate system to the Navier-Stokes equation these two dimensionless parameters are found.

$$\delta = \frac{a}{R} \tag{5-1}$$

$$\kappa = Re\sqrt{\delta} \tag{5-2}$$

The curvature ratio is the ratio of the pipe radius a (in earlier chapters called R_2) and the radius of the curved pipe, R . The Dean number is the dimensionless product of the Reynolds number and square root of the curvature ratio. In addition it can be expressed as the ratio of the square root of the product of the convective inertial forces and centrifugal forces to the viscous forces.

For the simulation of single-phase curved pipe flow three Reynolds numbers and Dean numbers have been used: $Re = 100, 300$ and 500 , $\kappa = 41, 122$ and 204 . By using different Reynolds numbers and Dean numbers it was possible to study the secondary flow and its influence on the total flow.

5-2 Basic equations

In order to derive the momentum equation for a curved-pipe flow the Navier-Stokes equation must be written in toroidal co-ordinates.

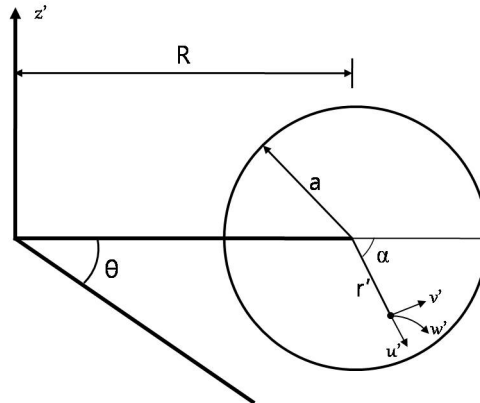


Figure 5-1: Toroidal co-ordination

In figure 5-1, u' , v' and w' are dimensionless velocities in a cross-section of the pipe in the radial, circumferential and axial direction respectively. θ is curvature angle of the curved pipe and α is the angle of a liquid particle located in the cross-section of the pipe. We introduce the following dimensionless quantities:

$$r = \frac{r'}{a}, \quad s = \frac{R\theta}{a}, \quad t = \frac{\overline{W}_0 t'}{a}, \quad u = \frac{u'}{\overline{W}_0}, \quad v = \frac{v'}{\overline{W}_0}, \quad w = \frac{w'}{\overline{W}_0}, \quad p = \frac{p'}{\rho \overline{W}_0^2} \quad (5-3)$$

where \overline{W}_0 is averaged axial velocity in the pipe and the Reynolds number can be formulated as the ratio of inertial force and viscous force, $\frac{a\overline{W}_0}{\nu}$. Using these quantities the equations of motion and continuity equation for an incompressible liquid in a toroidal coordinate system are given by [18]

radial momentum

$$\begin{aligned}
& \frac{\partial u}{\partial t} + \frac{1}{rB} \left[\frac{\partial}{\partial r}(rBu^2) + \frac{\partial}{\partial \alpha}(Buv) + \frac{\partial}{\partial \theta}(\delta ruw) - Bv^2 - \delta r \cos \alpha w^2 \right] \\
& = -\frac{\partial p}{\partial r} + \frac{1}{Re} \left[\frac{1}{rB} \left\{ \frac{\partial}{\partial r} \left(rB \frac{\partial u}{\partial r} \right) + \frac{\partial}{\partial \alpha} \left(\frac{B}{r} \frac{\partial u}{\partial \alpha} \right) + \frac{\partial}{\partial \theta} \left(\frac{\delta^2 r}{B} \frac{\partial u}{\partial \theta} \right) \right\} \right. \\
& \quad \left. - \frac{1}{r^2} \left(2 \frac{\partial v}{\partial \alpha} + u \right) + \frac{\delta \sin \alpha v}{rB} + \frac{\delta^2 \cos \alpha}{B^2} \left(v \sin \alpha - u \cos \alpha - 2 \frac{\partial w}{\partial \theta} \right) \right]
\end{aligned} \tag{5-4}$$

circumferential momentum

$$\begin{aligned}
& \frac{\partial v}{\partial t} + \frac{1}{rB} \left[\frac{\partial}{\partial r}(rBuv) + \frac{\partial}{\partial \alpha}(Bv^2) + \frac{\partial}{\partial \theta}(\delta rvw) + Buv + \delta r \sin \alpha w^2 \right] \\
& = -\frac{1}{r} \frac{\partial p}{\partial \alpha} + \frac{1}{Re} \left[\frac{1}{rB} \left\{ \frac{\partial}{\partial r} \left(rB \frac{\partial v}{\partial r} \right) + \frac{\partial}{\partial \alpha} \left(\frac{B}{r} \frac{\partial v}{\partial \alpha} \right) + \frac{\partial}{\partial \theta} \left(\frac{\delta^2 r}{B} \frac{\partial v}{\partial \theta} \right) \right\} \right. \\
& \quad \left. + \frac{1}{r^2} \left(2 \frac{\partial u}{\partial \alpha} - v \right) - \frac{\delta \sin \alpha u}{rB} - \frac{\delta^2 \sin \alpha}{B^2} \left(v \sin \alpha - u \cos \alpha - 2 \frac{\partial w}{\partial \theta} \right) \right]
\end{aligned} \tag{5-5}$$

axial momentum

$$\begin{aligned}
& \frac{\partial w}{\partial t} + \frac{1}{rB} \left[\frac{\partial}{\partial r}(rBuw) + \frac{\partial}{\partial \alpha}(Bvw) + \frac{\partial}{\partial \theta}(\delta rw^2) + \delta rw (u \cos \alpha - v \sin \alpha) \right] \\
& = -\frac{\delta}{B} \frac{\partial p}{\partial \theta} + \frac{1}{Re} \left[\frac{1}{rB} \left\{ \frac{\partial}{\partial r} \left(rB \frac{\partial w}{\partial r} \right) + \frac{\partial}{\partial \alpha} \left(\frac{B}{r} \frac{\partial w}{\partial \alpha} \right) + \frac{\partial}{\partial \theta} \left(\frac{\delta^2 r}{B} \frac{\partial w}{\partial \theta} \right) \right\} \right. \\
& \quad \left. + \frac{2\delta^2}{B^2} \left(2 \frac{\partial u}{\partial \theta} \cos \alpha - \frac{\partial v}{\partial \theta} \sin \alpha - \frac{w}{2} \right) \right]
\end{aligned} \tag{5-6}$$

continuity

$$\frac{\partial}{\partial r}(rBu) + \frac{\partial}{\partial \alpha}(Bv) + \frac{\partial}{\partial \theta}(\delta rw) = 0 \tag{5-7}$$

(* $B = 1 + \delta r \cos \alpha$)

5-3 Boundary conditions

We solved the single phase flow equations numerically using the OpenFoam code for the 90° bend shown in figure 5-2. The curvature ratio of the curved bend is $\delta=1/6$. For the numerical solution we needed the boundary conditions at the inlet, outlet and pipe wall. The inlet is vertical and the flow acts against gravity in that part. At the wall the no-slip condition holds. The outlet part is horizontal. The fully developed parabolic velocity profile is imposed at the inlet and initial velocity condition, while the natural (zero-gradient) outflow condition is used.

5-4 Single Phase flow in 90° bend

We selected five cross-section areas at $\theta = 0, \pi/8, \pi/4, 3\pi/8$ and $\pi/2$ in the 90° bend to analyse the flow patterns in these cross-sections of the pipe (see figure 5-2). We selected three cases of Reynolds number, $Re = 100, 300$ and 500 , and Dean number, $\kappa = 41, 122$ and 204 . We paid special attention to the secondary flows and the position of the point of maximum axial velocity. The results are compared with finite-element method (FEM) calculations for $Re = 100, 300$ and 500 of Vosse et al [7] and with experimental data at $Re = 300$ derived by Bovendeerd [7].

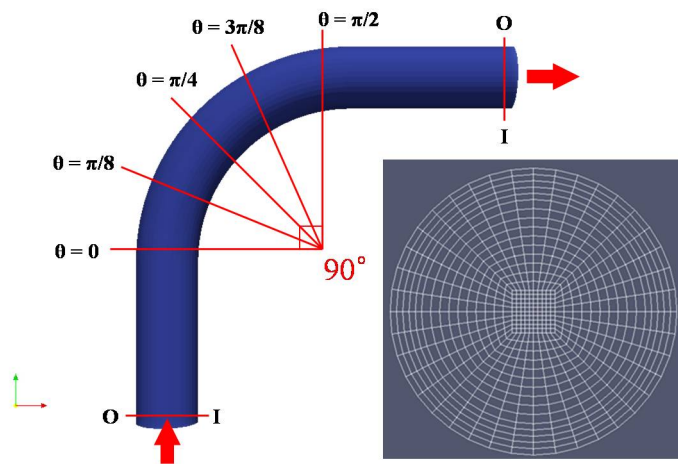


Figure 5-2: Geometry of 90° bend. Indicated angles are the location of cross sections for analysis

5-4-1 Axial velocity distribution

In figure 5-3 the axial velocity distribution in a number of pipe cross-sections is shown for three values of the Reynolds number. A comparison is made with the numerical results of van de Vosse and with experimental results of Bovendeerd. As can be seen in figure 5-3 the agreement is good. At the inlet of the pipe the location of the maximum velocity is at the pipe centerline. However in the curved part of the pipe this location starts moving to the outer-curve part of the pipe. This effect depends on the Reynolds number. With increasing Reynolds number the shift in the location of maximum velocity becomes stronger.

The deformation of the axial velocity distribution from the parabolic profile in the curved part of the pipe depends also on the Reynolds number. At a Reynolds number of 100 the deviation from the parabolic profile remains limited. However for values of the Reynolds number of 300 and 500 the velocity distribution deviates considerably from the parabolic profile. This is in accordance with the results for the location of maximum axial velocity.

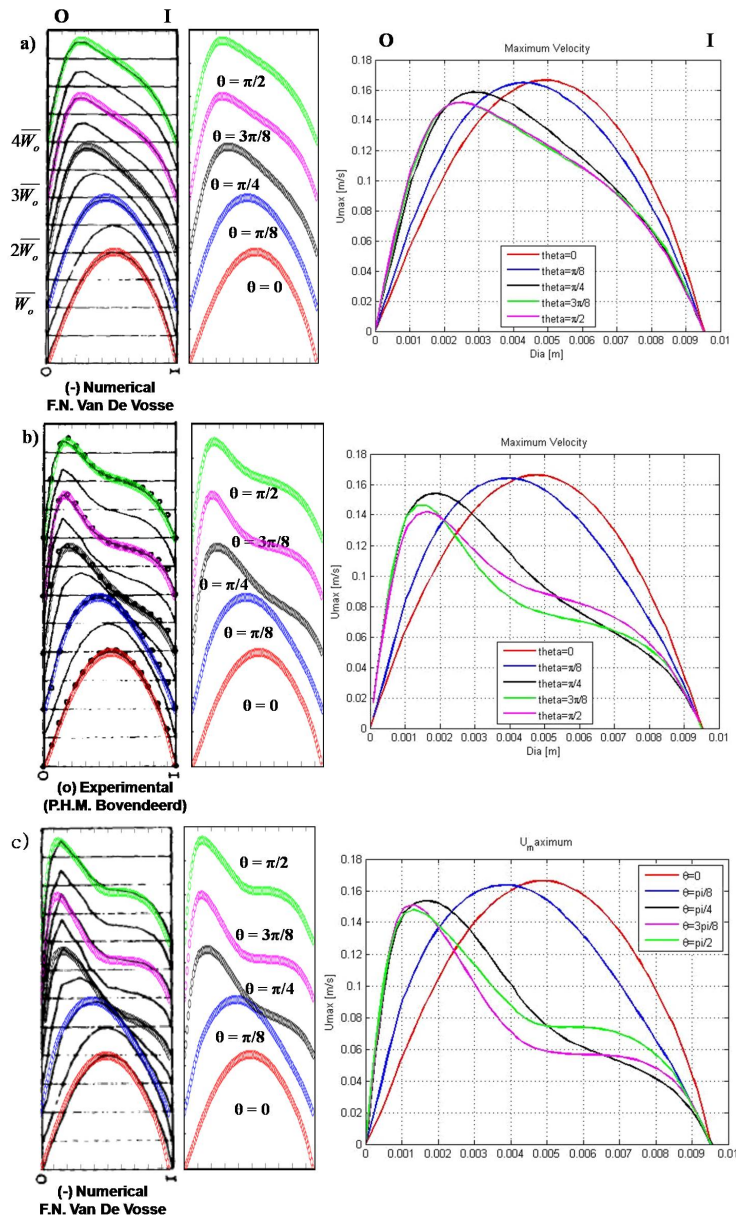


Figure 5-3: Axial velocity at $Re =$ a) 100, b) 300 and c) 500. The results presented as the thin black line of the figure were derived by Vosse et al. (a and c)[7] and by Bovendeerd et al.(b) [8] (I: inner curve, O: outer curve)

5-4-2 Contour plots for axial velocity distribution

In figure 5-4 contour plots are given for the axial velocity distribution in pipe cross-sections for three values of the Reynolds number and five consecutive cross-sections in the curved part of the pipe. In the top half of the plots the numerical and experimental results of respectively van de Vosse and Bovendeerd are shown, In the bottom half our numerical results are shown. As can be seen the agreement is good. Also these plots show the considerable deformation of the velocity profile in the curved part of the pipe and the shift in the location of maximum

axial velocity. This effect becomes stronger with increasing Reynolds number.

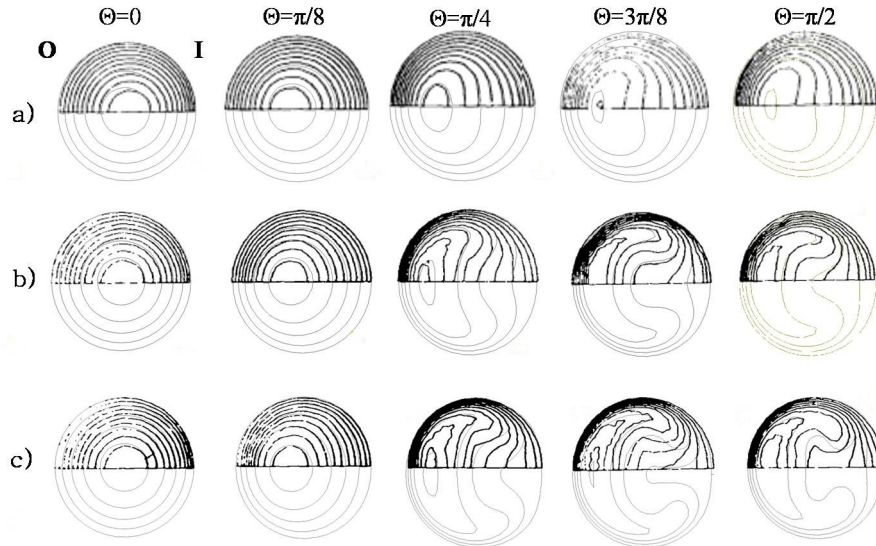


Figure 5-4: Axial velocity contour maps; a) $Re = 100$, b) 300 and c) 500, (I: inner curve, O: outer curve). The results presented in the upper half of the figure were derived by Vosse et al. (a and c)[7] and by Bovendeerd et al.(b) [8] Our numerical results are given in the bottom half.

5-4-3 Secondary flow velocity

In order to analyse the physical characteristic of the flow field more in detail we also paid attention to the secondary velocity components perpendicular to the pipe axis. The results are shown in figure 5-5 at the end of this chapter. Enlarged versions of the secondary flows are given in figure 5-6, figure 5-7 and figure 5-8 at the end of this chapter. At the inlet to the pipe no secondary flows are observed. However in the curved part of the pipe secondary flows develop. The highest secondary flow is observed at $\theta = \pi/4$. At the centreline the flow is from the inner-curve part of the pipe to the outer-curve part. The flow then continues from the outer-curve part downward along the pipe wall back to the inner-curve part. So two vortices are present. At the higher Reynolds number ($Re = 300$ and 500) the location and shape of vortices are rather similar to those for the low Reynolds number case ($Re = 100$). So it seems that the Reynolds number does not have a strong influence on the shape and location of the vortices, although with increasing Reynolds number the location of vortices shifts slightly more to the inner-curve part of the pipe. However the magnitude of the secondary flow velocity is stronger at higher Reynolds numbers than at lower value of the Reynolds number.

5-4-4 Conclusion

In this chapter we studied the single-phase flow of liquid through a 90° bend at three values of the Reynolds number (100, 300, and 500). We compared our numerical results with those of van de Vosse et al. and with the experimental data of Bovendeerd et al. Our results compared well with the literature data. Special attention was given to the axial velocity distribution and the shift of the maximum axial velocity due to the curvature. The parabolic profile changes its shape in the curved part of the pipe. This deformation is strongest at the highest value of the Reynolds number. A secondary flow perpendicular to the pipe axis occurs in the bend. It flows upward through the centre of the pipe and downward again along the pipe wall. The strength of these vortices increases with increasing Reynolds number, but their shape remains nearly the same.

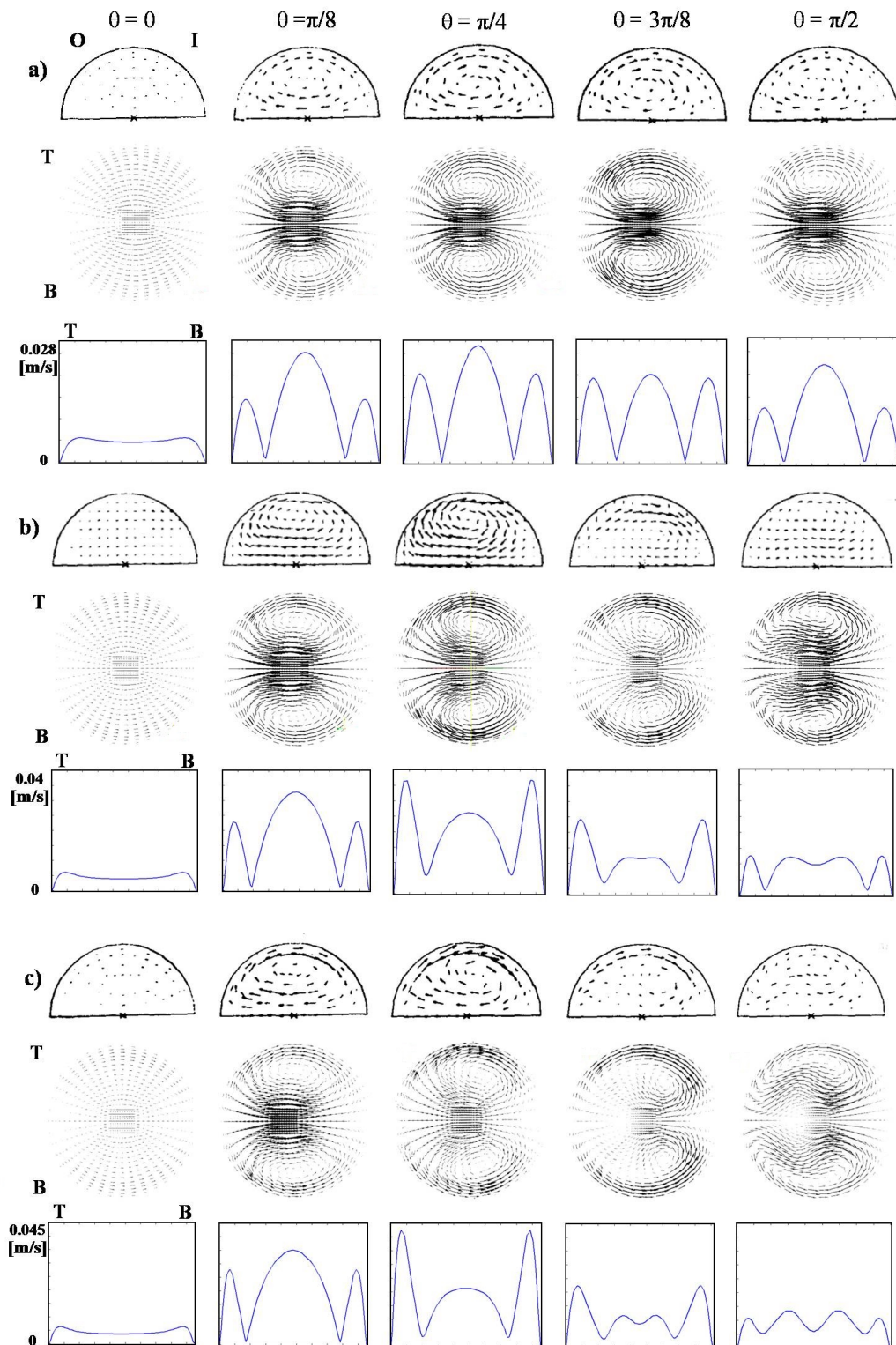


Figure 5-5: Secondary velocity: a) $Re = 100$, b) 300 and c) 500. The results presented in the upper half of the figure were derived by Vosse et al (a and c)[7] and by Bovendeerd et al (b) [8]. The full cross-section results are our numerical simulations.

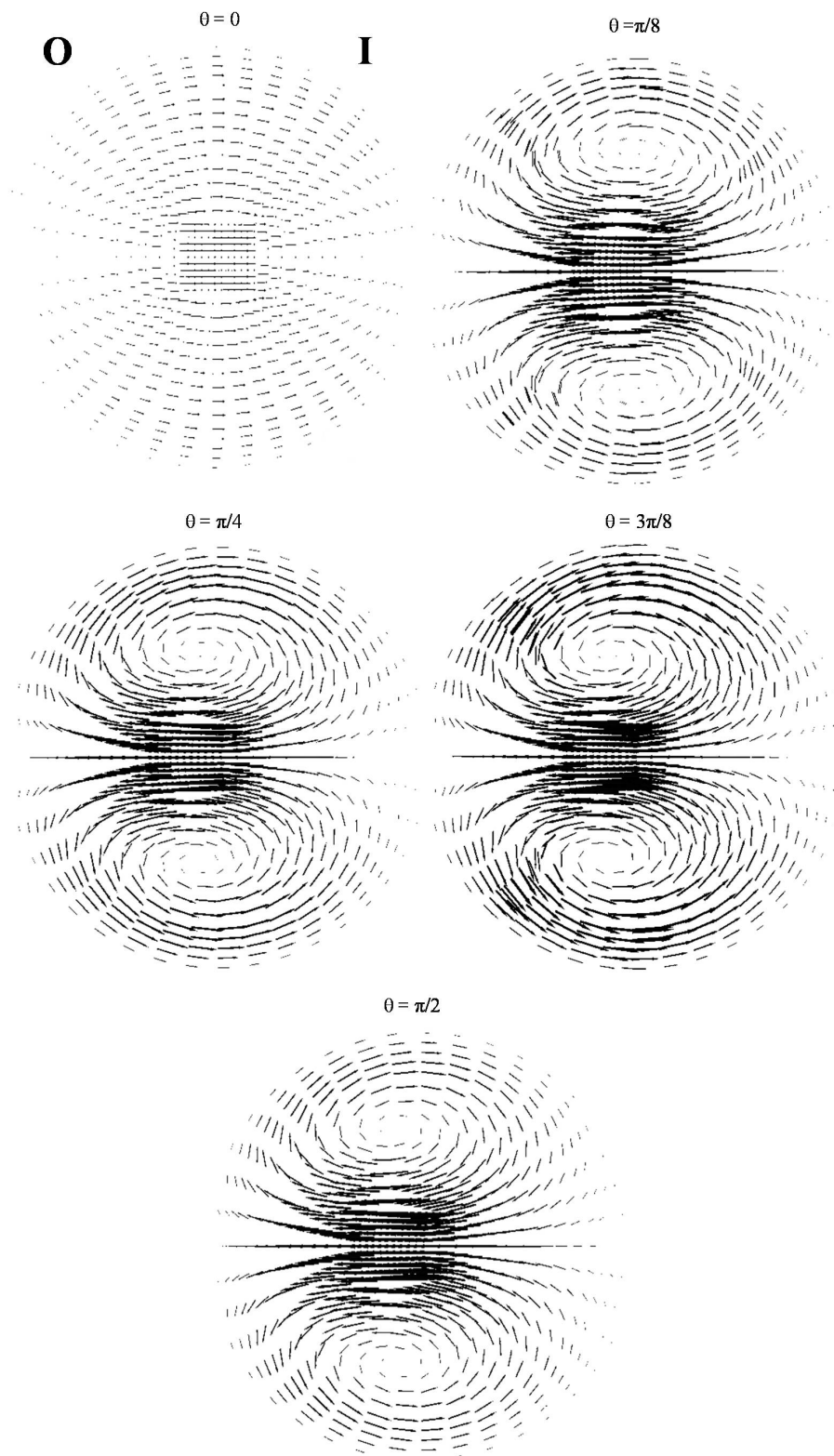


Figure 5-6: Enlarged version of secondary flows, $Re = 100$

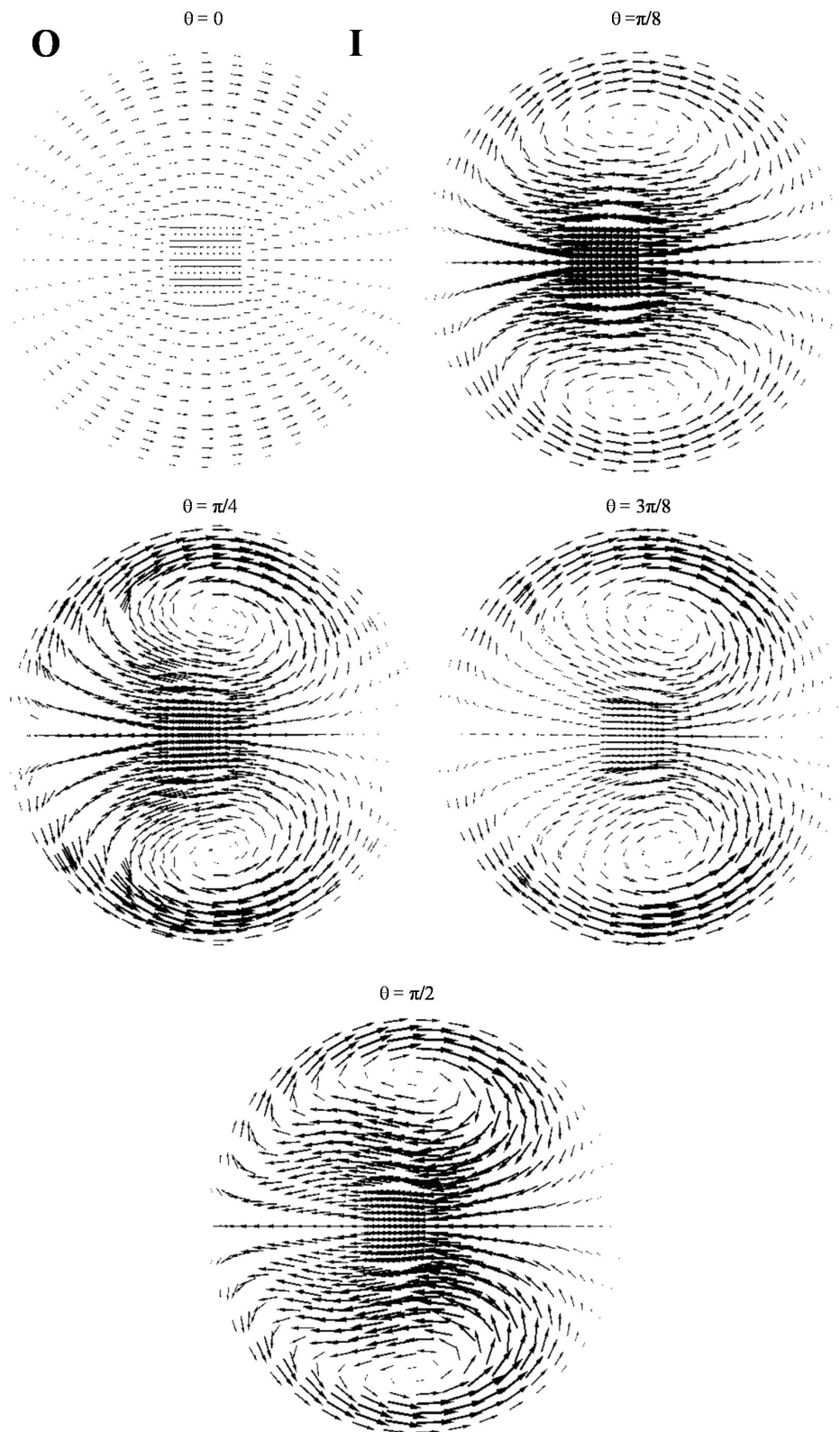


Figure 5-7: Enlarged version of secondary flows, $Re = 300$

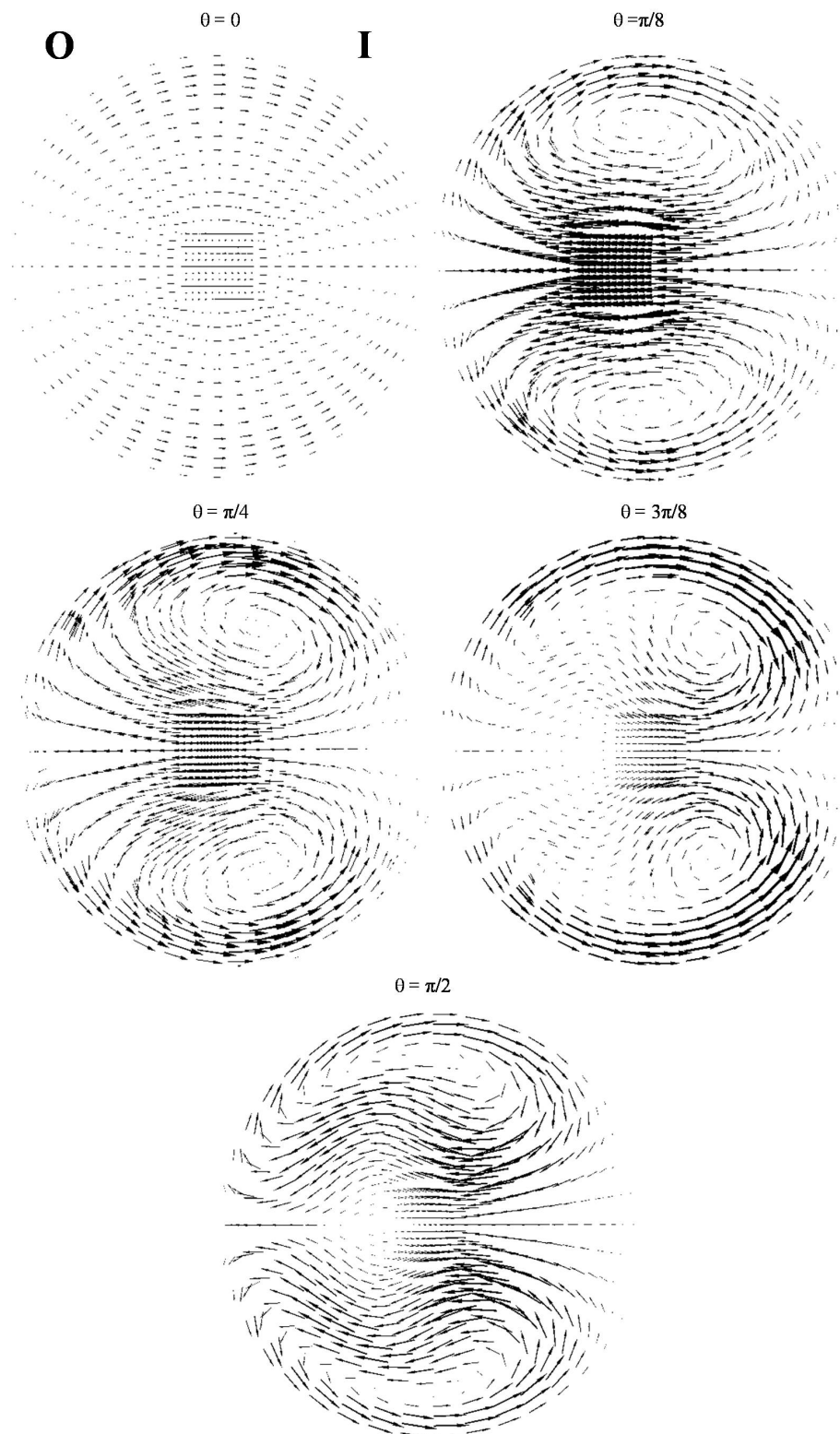


Figure 5-8: Enlarged version of secondary flows, $Re = 500$

Chapter 6

Core-Annular Flow in a 90° bend

After our study of single-phase flow through a 90° bend we extended it to core-annular flow in a 90° bend. Much research has been carried out on core-annular flow through a straight (vertical or horizontal) pipe, but not much on core-annular flow in a curved pipe. For the case of core-annular flow in a straight pipe special attention was given to the formation of waves at the core-annular interface. In our study we do not pay attention to this phenomenon. In case of core-annular flow through a straight pipe periodic boundary conditions can be applied to the inlet and outlet of the pipe. In the case of a curved pipe that is no longer possible. So inlet and outlet conditions have to be supplied. With periodic boundary conditions the length of the computation domain can be restricted to a rather short pipe length and the calculation can be continued until convergence has been reached. With inlet and outlet conditions a long pipe length is needed for the computation domain before convergence is reached. The flow will also not remain axi-symmetric, so a three dimensional computation domain has to be applied. These facts make the computation time much longer then for the case that periodic boundary conditions can be used. In this chapter we give results for the change in the shape of the core due to the curvature effect (centrifugal force) and for the secondary flow development. First we neglect the influence of the buoyancy force on flow due to the density difference between the core liquid (oil) and the annular liquid (water). Next we included the gravity effect and studied its influence on core-annular flow.

6-1 Geometry and boundary condition

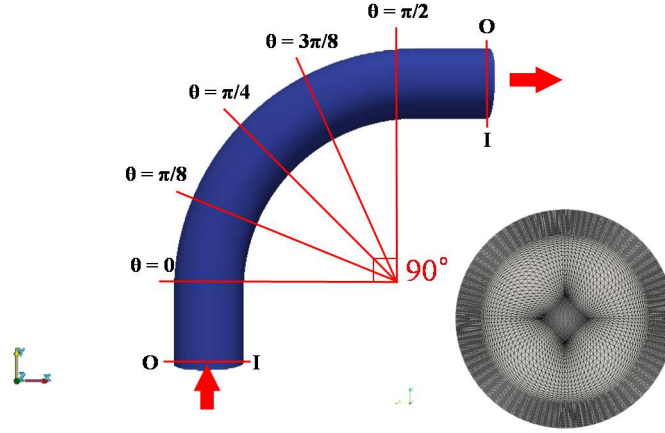


Figure 6-1: Geometry for core-annular flow in a 90° bend, Indicated angles are the location of cross sections for analysis

We used the same 90° bend as for the single-phase flow in the foregoing chapter (see figure 6-1). The pipe radius was $R_2 = 0.00476 \text{ m}$. As velocity distribution at the inlet we used the analytical expression of Li and Renardy for a fully developed velocity profile. Close to the pipe wall is the thin layer of water, where the largest gradients in velocity can be expected. In that region the computation mesh was finer than at the pipe center. In total 412412 cells were used; 4532 in cross-sectional direction and 91 in the axial direction.

6-2 Core-annular flow in a 90° bend without buoyancy effect

Ooms et al[6] already studied horizontal core-annular flow in the straight pipe without buoyancy effect. Here we will use the same parameters as used by Ooms et al[6], but this time for the flow through a 90° bend. By neglecting the buoyancy effect we can concentrate on the influence of the centrifugal force on the flow in the curved part of the pipe. The physical parameters are given by $\rho_o = 905 \text{ kg/m}^3$, $\rho_w = 995 \text{ kg/m}^3$, $\mu_o = 0.601 \text{ kg/m} \cdot \text{s}$, $\mu_w = 0.001 \text{ kg/m} \cdot \text{s}$, $\sigma^* = 8.54 * 10^{-3} \text{ kg/s}^2$, $R_1 = 0.00372 \text{ m}$ and $f^* = 150 \text{ kg/m}^2$, which gives the following values of the relevant dimensionless groups

$$m = 0.00166, \quad a = 1.28, \quad \zeta = 1.10, \quad K = 1, \quad J = 7.96 * 10^{-2}, \quad Re_1 = 1.85, \quad \kappa_1 = 0.755, \quad (6-1)$$

in which κ_1 is the Dean number. As mentioned we assumed that at the inlet a smooth core-annular flow velocity distribution according to Li and Renardy is present. This distribution was also supposed to be present inside the pipe at the start of the calculation.

6-2-1 Core shape and position in the pipe

We first studied the location of the core inside the pipe at a number of pipe cross-sections as function of time. In particular we were interested to find out, whether fouling of the pipe

wall occurred due to touching of the wall by the oil core. In figure 6-2 presented on next page the core position inside the pipe is shown for a number of cross-sections and time steps. More detailed information about the core position is given in the bottom part of the figure. It can be seen that the core position is quickly established in time. At the inlet the core has an axisymmetric shape. However further down the pipe the core starts to deform and move to the outer-curved part of the pipe. However it never touches the wall. As we will show later this is due to the pressure build-up in the annular layer which pushes the core from the wall. As oil has a lower density than water we expected that the core would move to the inner-curved part of the pipe. In order to explain this surprising phenomenon we studied the secondary flows perpendicular to the pipe axis.

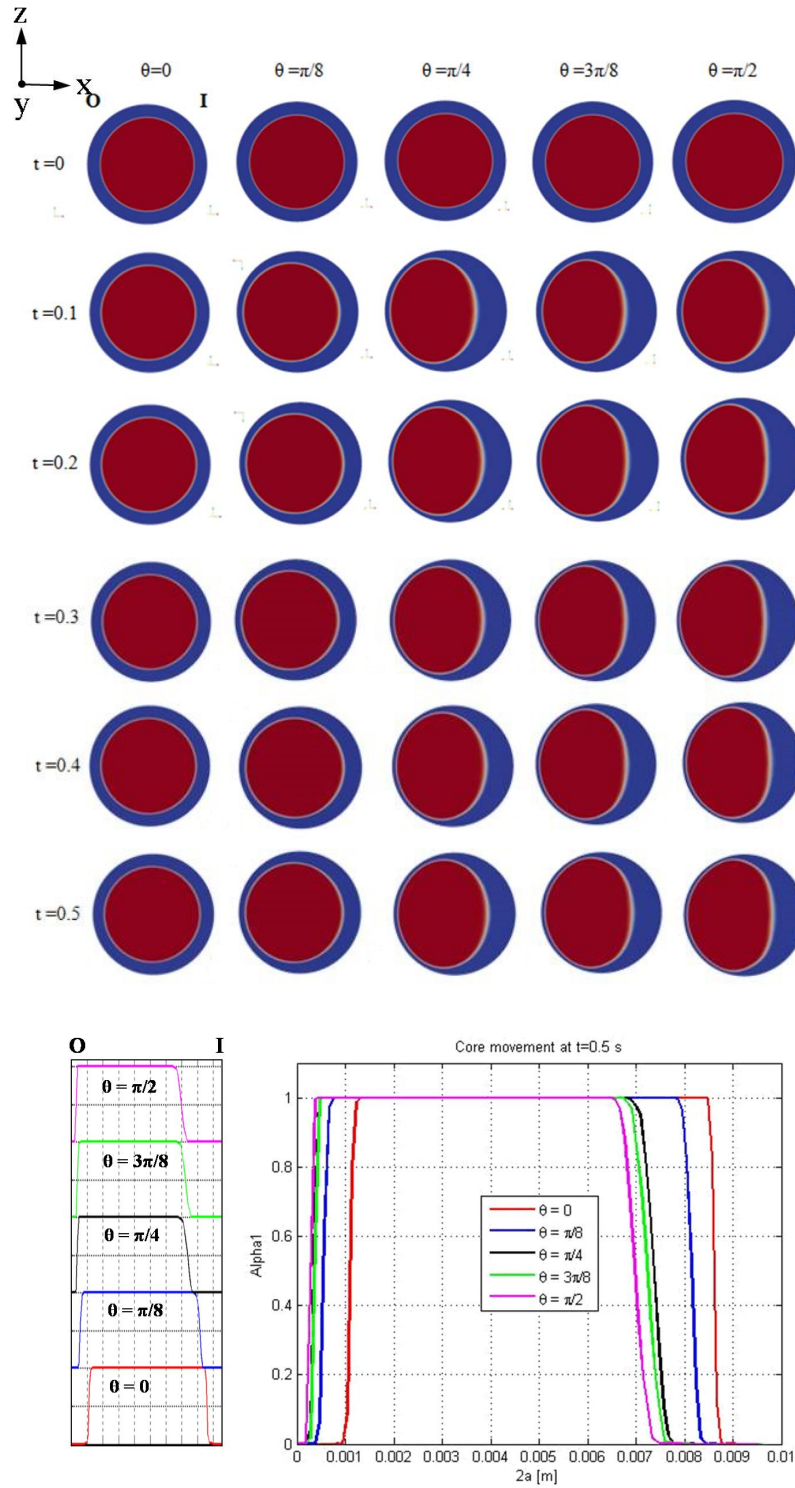


Figure 6-2: Different position of the oil core inside the pipe. Red and blue colors in the contour map indicate oil and water, respectively. (I: inner curve, O: outer curve)

6-2-2 Axial and secondary flows

In the case of single-phase flow we already found the development of secondary flows perpendicular to the pipe axis in the curved part of the pipe. This is also the case for core-annular flow, but this time the situation is more complicated. We start with a discussion of the axial velocity distribution in the pipe. In figure 6-3 this distribution is given for a number of axial positions in the bend. At the inlet the core velocity is nearly constant due to the large viscosity of the oil compared to the water viscosity. In the water annulus the velocity decreases quickly from the core velocity to zero velocity at the pipe wall. However in the curved part of the pipe the core moves to the outer wall and the core velocity is no longer constant. At the outer-curved part of the pipe the velocity becomes larger than at the inner-curved part. The highest axial velocity was found at $\theta = \pi/4$: $V_{max} = 0.35$ m/s. From the velocity distribution

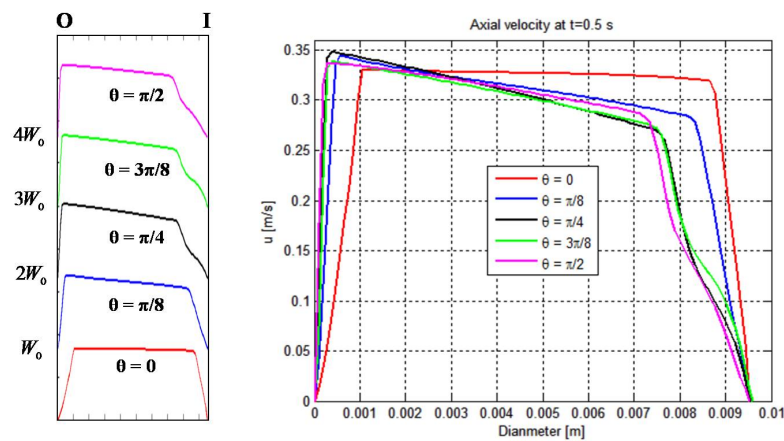


Figure 6-3: Axial velocity distribution for core-annular flow in a bend. (I: inner curve, O: outer curve)

a rough estimate can be made of the centrifugal force distribution by taking the ratio of the square of the axial velocity and the radius of the pipe curvature. The result is given in Figure 6-4. The centrifugal force is largest at the outer-curved part of the pipe. The change in the

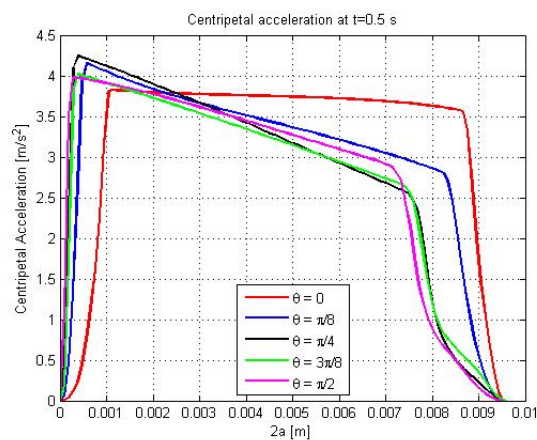


Figure 6-4: Centrifugal force distribution

position of the maximum axial velocity and the core deformation are more clearly visible in the axial velocity contour map (see figure 6-5). At $\theta = 0$ the axial velocity profile of the core is almost constant due to the high viscosity of the oil compared to the water viscosity, while in the annulus the velocity decreases nearly linearly to zero at the wall. Going in downstream direction the core starts deforming and the axial velocity profile in the annulus at the inner-curved part of the pipe is no longer linear. Due to the shear at the core-annular interface secondary flows could also be expected inside the core. However they were not observed, very likely due to the high viscosity of the oil compared to the water viscosity.

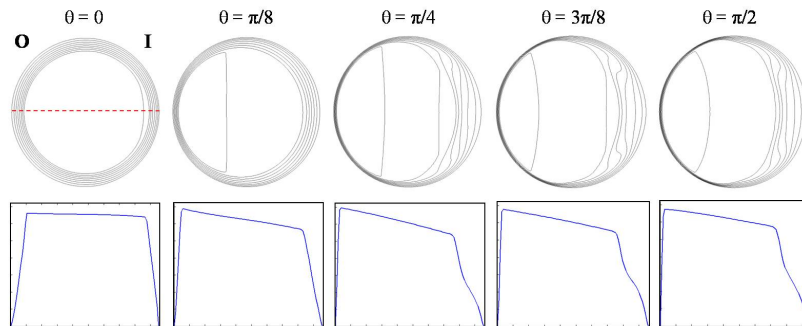


Figure 6-5: Axial velocity contour map and axial velocity distribution at $t = 0.5$ s (I: inner curve, O: outer curve)

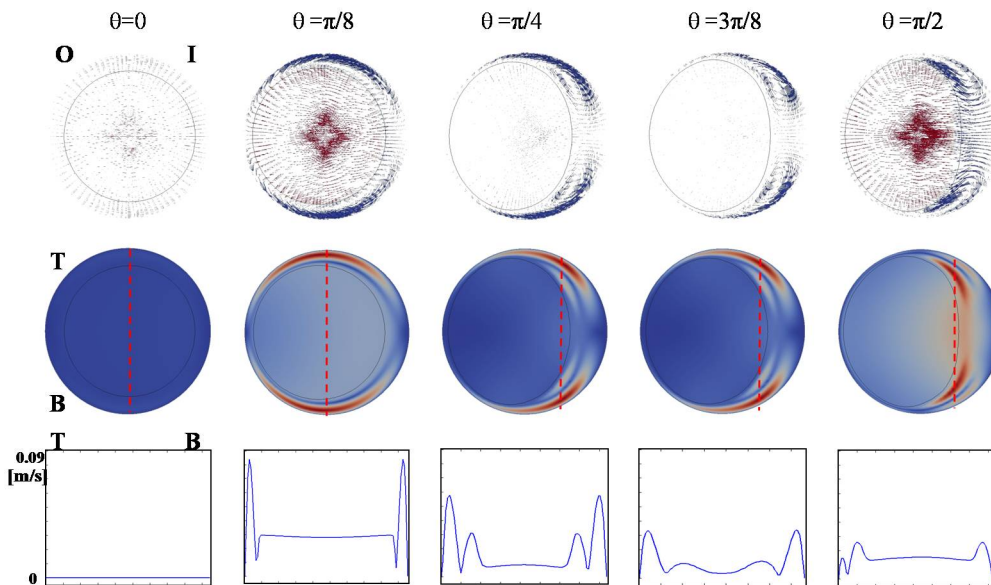


Figure 6-6: Secondary flows of core-annular flow at $t = 0.5$ s (I: inner curve, O: outer curve, T: Top of the cross section, B: Bottom of the cross section)

In figure 6-6 the secondary flows are shown that developed inside the water annulus. The recirculating flow in the annulus is upward along the core-annular interface and downward along the pipe wall. Of course, at the inlet the secondary flow does not exist. However when the flow enters the curved part of the pipe the secondary flow appears. At first it is rather weak, but it increases in strength on its way to the exit. The highest secondary flow is observed

at $\theta = \pi/8$. It pushes the core and therefore also the position of maximum axial velocity in the direction of the outer-curved part of the pipe. As can be seen the core also deforms on the influence of the secondary flow. The cross-sectional area for the vortices increases in the downstream axial direction. Enlarged versions of the secondary flows are shown in figure 6-16 at the end of the chapter.

6-2-3 Pressure distribution

Although the core moves under the influence of the centrifugal force to the outer-curved part of the pipe, it does not touch and foul the pipe wall. This is caused by the pressure build-up at that part of the pipe, as can clearly be seen in figure 6-7 and figure 6-8. At the inlet of the pipe the pressure in the core is slightly higher than in annulus due to the interfacial tension. In downstream direction the pressure distribution changes strongly. The pressure at the outer-curved part of the pipe increases, whereas it decreases at the inner-curved part. So a net force is exerted on the core, pushing it away from the outer-curved part. This is the reason that fouling does not occur, although the annular film at the outer-curved part becomes rather thin. It is very well possible that at other flow conditions fouling takes place, but that requires a further study.

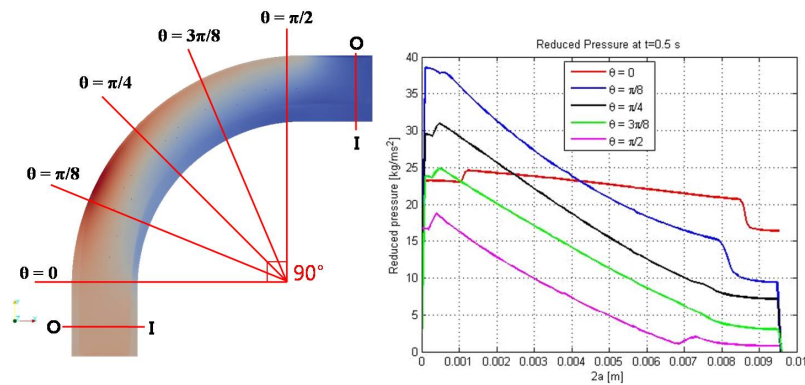


Figure 6-7: Pressure distribution of core-annular flow at $t = 0.5$ s (I: inner curve, O: outer curve)

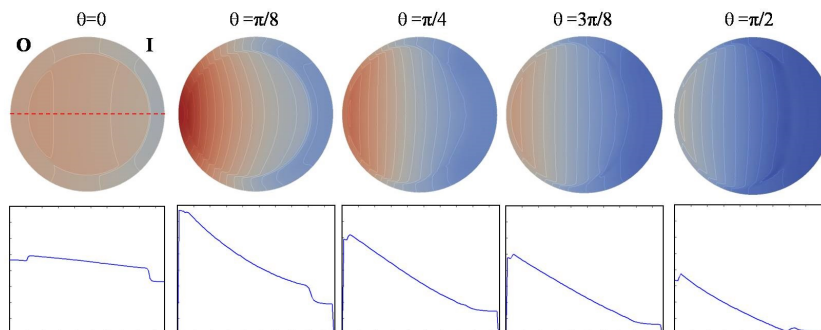


Figure 6-8: Pressure distribution of the two phase flow at $t = 0.5$ s without gravity effect. (I: inner curve, O: outer curve)

6-3 Core-annular flow in a 90° bend with buoyancy effect

In the preceding section we presented core-annular flow without buoyancy effect to study the influence of the centrifugal force on core-annular flow in a curved pipe. In this section we present the same study but now with buoyancy effect. The 90° bend is the same as in the foregoing case. We assume that the bend lies in a horizontal plane and that the gravity force is perpendicular to it, so perpendicular to the axial flow direction (see figure 6-9). Apart from the gravity force the flow conditions are the same as in the previous case.

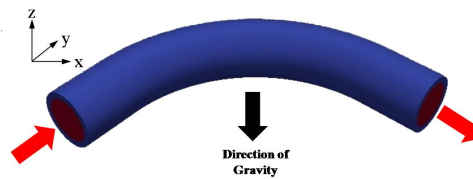


Figure 6-9: Geometry of the case with buoyancy effect

6-3-1 Core shape and position in the pipe

In figure 6-10 we give a sketch of the forces acting on the core. The centrifugal force is in the x-direction and the gravity force in the z-direction. So the combined force is no longer in the x-direction, but makes an angle with it.

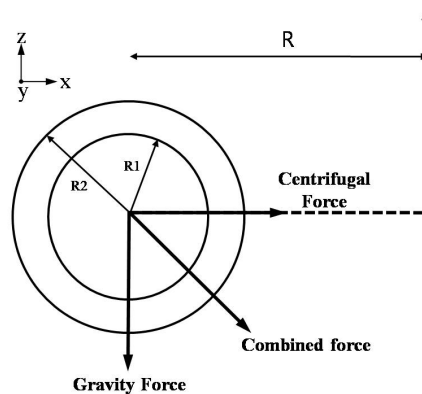


Figure 6-10: Sketch of the combined force due to the centrifugal force and gravity force

For that reason the core shape and position in the pipe is different than for the case without

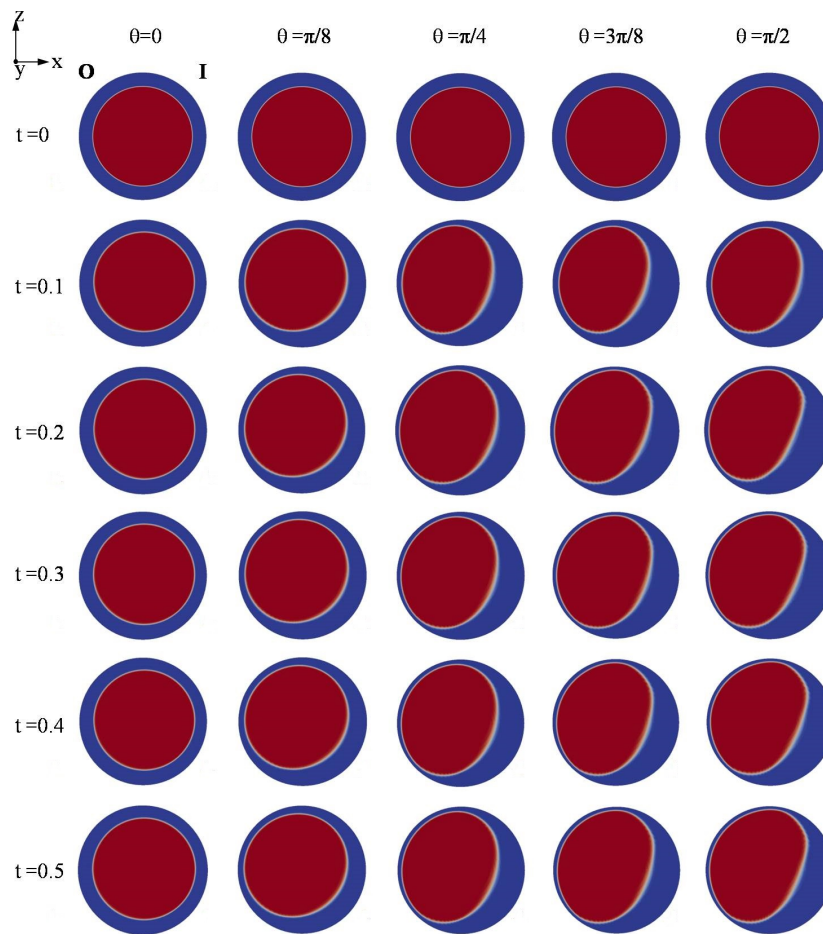


Figure 6-11: Different core shape and position of core-annular flow in a bend with gravity force. Red and blue color in contour map is oil and water, respectively. (I: inner curve, O: outer curve)

gravity force. The core shape and position as function of time for different cross-sections along the pipe are shown in figure 6-11. At the inlet the core is axisymmetric. However in the curved part of the pipe it moves slightly upwards and in the direction of the outer-curved part of the pipe and the core shape changes significantly. This is again due to the action of the secondary flows (to be discussed). It can be seen that the equilibrium position of the core in the pipe is quickly established. At $\theta = \pi/4$ there is no significant change in the shape and position of the core. Fouling was again not observed.

6-3-2 Axial and secondary flows

Axial velocity

Axial velocity contour plots and axial velocity distributions for different cross-sections along the pipe are given in figure 6-12. The core velocity is at the inlet almost constant due to the

large viscosity of the core liquid (oil) compared to the viscosity of the annulus liquid (water). However due to the movement of the core in the direction of the outer-curved part of the pipe, the shear at the core-annular interface increases significantly at that part of the pipe and so the velocity distribution changes also. It can be seen that the velocity distribution is different from the case without buoyancy. This is due to the fact that the core moves to the outer-curved part of the pipe in a direction that makes an angle of about 30° with the x-direction. The axial velocity is again highest close to the thinnest part of the annulus.

Secondary flows

In figure 6-13 the secondary flow and the iso-axial velocity contour lines are shown. At the inlet no secondary flows are present. However with increasing distance in axial direction secondary flows develop and the highest secondary flow is observed at $\theta = \pi/8$. At first two rather weak vortices appear at the top and bottom side of the core. Further down in axial direction a peculiar phenomenon occurred: the vortex at the top side becomes weaker and the one at the bottom side increases in strength. Finally only the bottom side vortex remains and becomes still stronger. The flow at the core-annular interface is upward to the outer curve of the pipe and downward along the pipe wall. As in the case without gravity force the secondary flow pushes the core to the outer curve of the pipe and causes the rather strong deformation of the core shape. Enlarged versions of the secondary flows are shown in figure 6-17 at the end of the chapter.

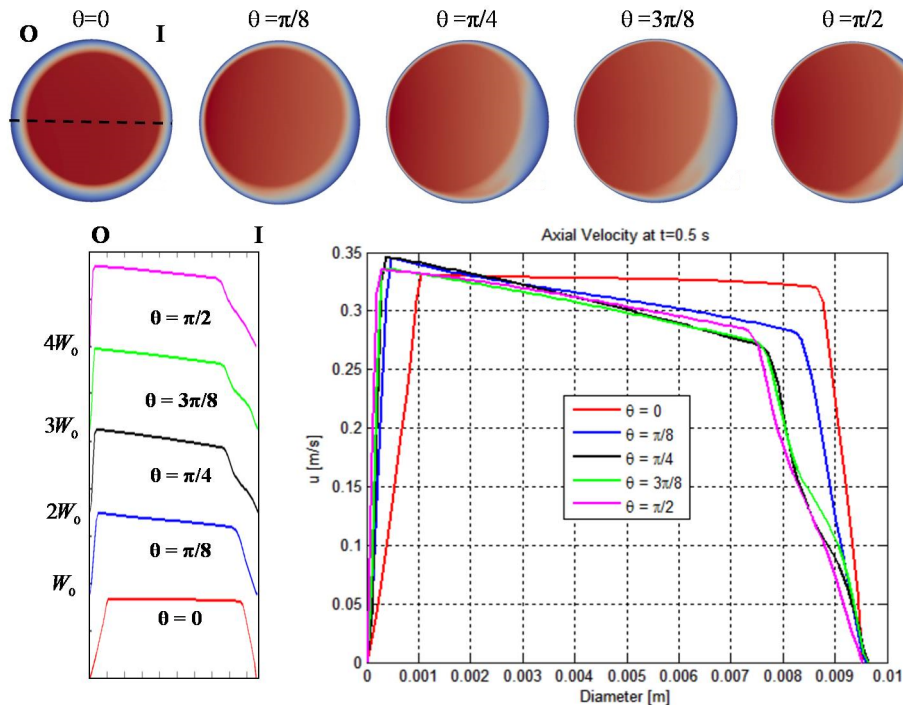


Figure 6-12: Axial velocity contour plots and axial velocity distributions for core-annular flow in a bend with gravity effect (I: inner curve, O: outer curve)

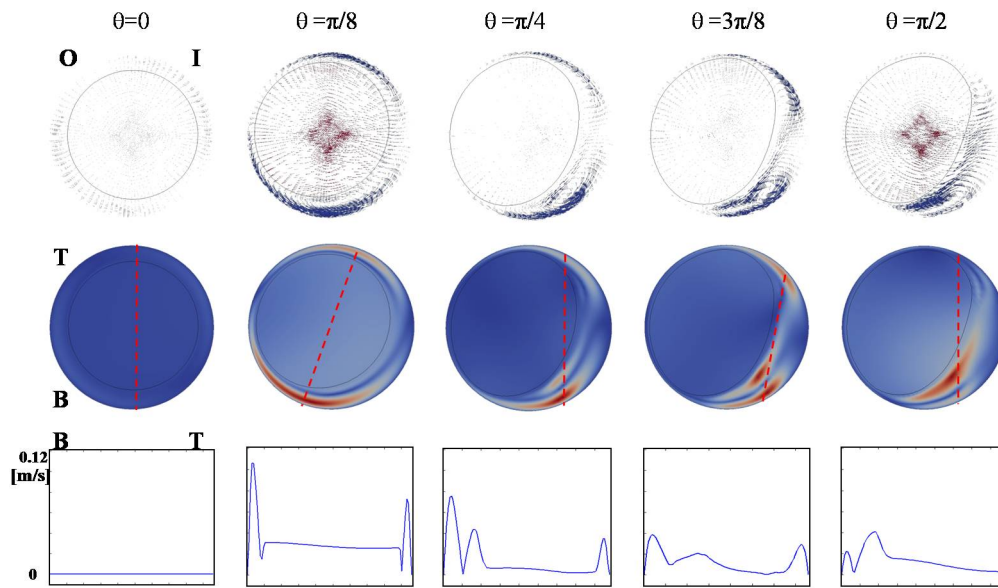


Figure 6-13: Secondary flows and iso-axial velocity contour lines for core-annular flow in a 90° bend with gravity effect. (I: inner curve, O: outer curve, T: Top of the cross section, B: Bottom of the cross section)

6-3-3 Reduced pressure

In figure 6-14 and figure 6-15 the reduced pressure distribution and reduced pressure contour plots are given at several cross-sections of the pipe. The reduced pressure is the pressure without the gravity contribution. The result is rather similar to the one for the case without gravity effect, although due to the combined action of centrifugal force and gravity force the pressure is slightly larger. The highest values of the pressure are found at the upper-curved part of the pipe. This is due to the secondary flow, that pushes the core in the upper-curved part. The highest pressure is found at the curvature angle $\theta = \pi/8$. The large pressure built-up at the upper-curved part of the pipe is responsible for the fact that the core does not touch and foul the pipe wall. The difference in pressure between the core and the annulus which is clearly visible in figure 6-15.

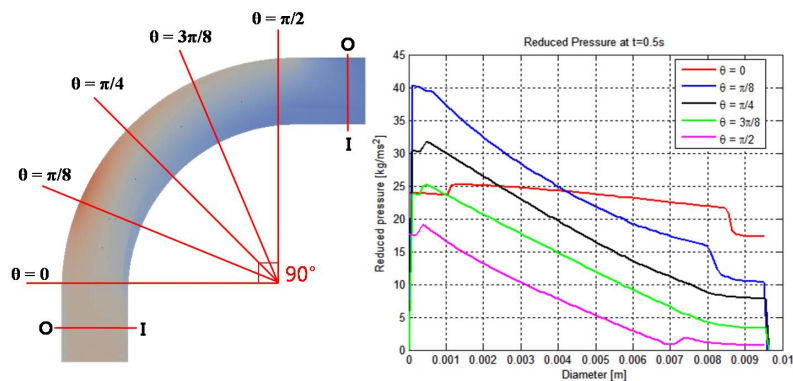


Figure 6-14: Reduced pressure distribution at $t = 0.5$ s at several cross-sections of the pipe

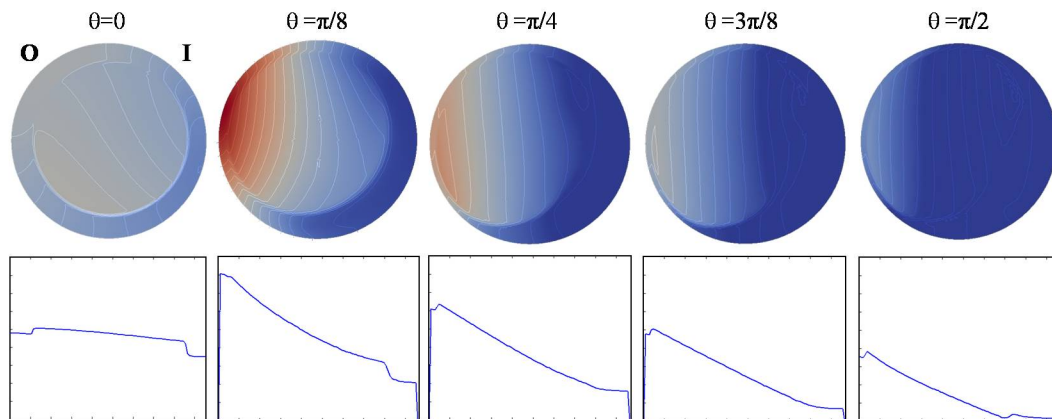


Figure 6-15: Reduced pressure contour plots at $t = 0.5$ s at several cross-sections of the pipe

6-4 Conclusion

In this chapter we studied two cases of core-annular flow in a bend: first without gravity effect and then with gravity. In this way we could separate the effect of the centrifugal force and the gravity force on the flow. We found that secondary flows occurred in the annular layer which push the core to the outer-curved part of the pipe. Without gravity the movement of the core to the wall is symmetric with respect to the x -axis; for the case with gravity effect the core movement is slightly upward and no longer symmetric with respect to the x -axis. Without gravity there are two vortices in the annular layer that are also symmetric with respect to the x -axis. With gravity a peculiar effect occurs: the top side vortex becomes weaker in the axial flow direction and finally disappears, whereas the bottom side vortex survives and becomes stronger. This causes the non-symmetric movement of the core with respect to the x -axis. At the outer-curved part of the pipe a high pressure build-up takes place. Therefore the core remains free from the pipe wall and does not foul it.

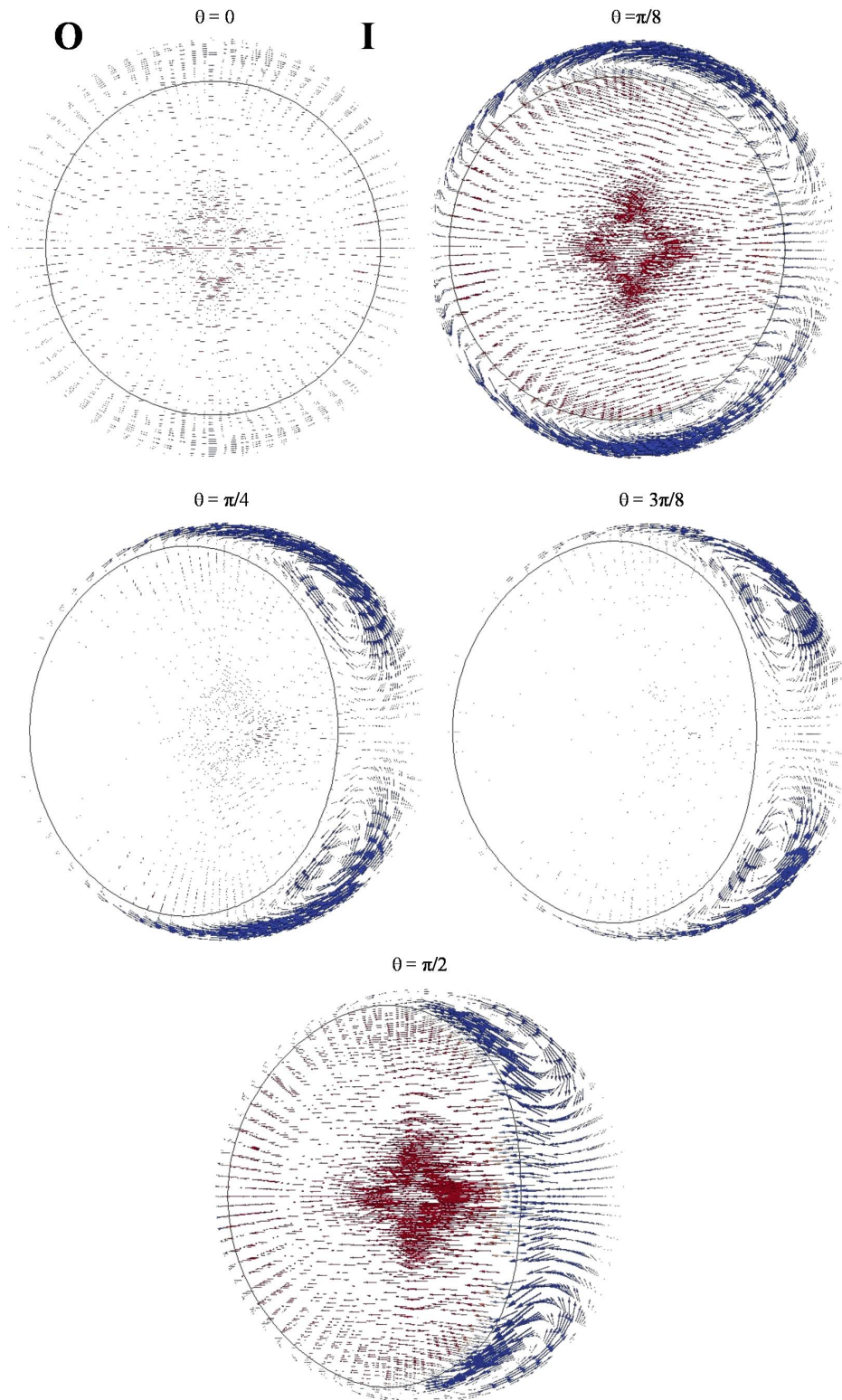


Figure 6-16: Enlarged version of secondary flow without buoyancy effect. The black circle line is interface between oil and water. (I: inner curve, O: outer curve)

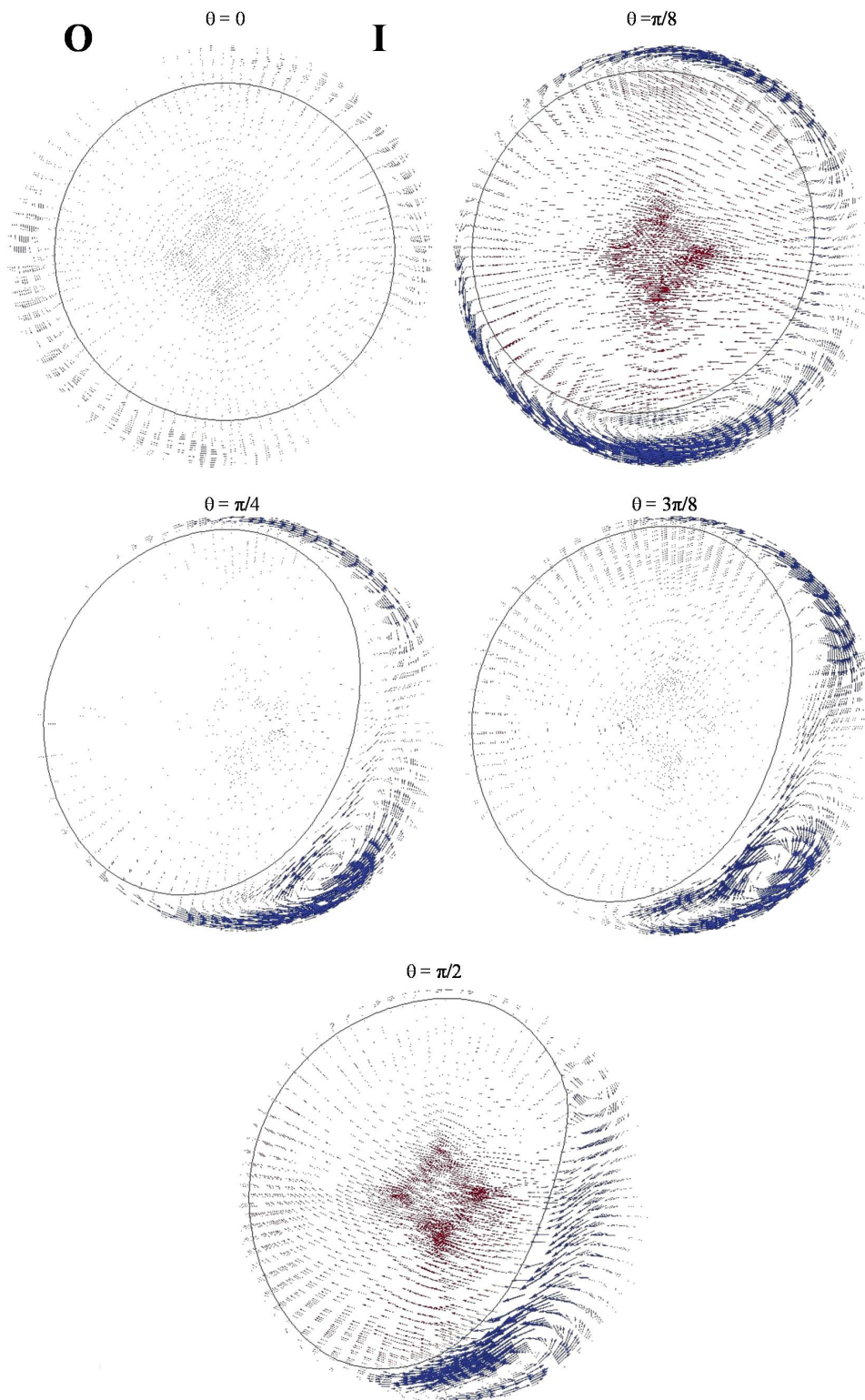


Figure 6-17: Enlarged version of secondary flow with buoyancy effect. The black circle line is interface between oil and water. (I: inner curve, O: outer curve)

Core-annular flow in 180° return bend

7-1 Introduction

In order to extend our study of core-annular flow in a curved pipe we studied also the flow in a 180° return bend. We compared our results with the experimental data of Sharma et al [9], who studied core-annular flow in a 180° return bend in up-flow, down-flow and horizontal flow with a curvature ratio of $(R/R_2) = 16.67$ and pipe radius of $R_2 = 0.006$ m. They studied a range of superficial oil and water velocity, $u_{s,o}^*$ and $u_{s,w}^*$, that belonged to a range of two-phase flow patterns such as droplet flow, core-annular flow, plug flow and distorted plug flow (see figure 7-1). From this range of superficial velocities we compared our predictions with the experimental flow for $u_{s,o}^* = 0.5$ m/s and $u_{s,w}^* = 0.5$ m/s that belonged to core-annular flow. In the experiments the straight parts at the inlet and outlet of the return bend were 340 times the pipe diameter. So very likely a wave was present at the core-annular interface during the experiments. Because of computation time such inlet and outlet lengths were not possible in our simulations. We choose an inlet and outlet length of 5 times the pipe diameter. We assumed a smooth core-annular interface; no waves were present.

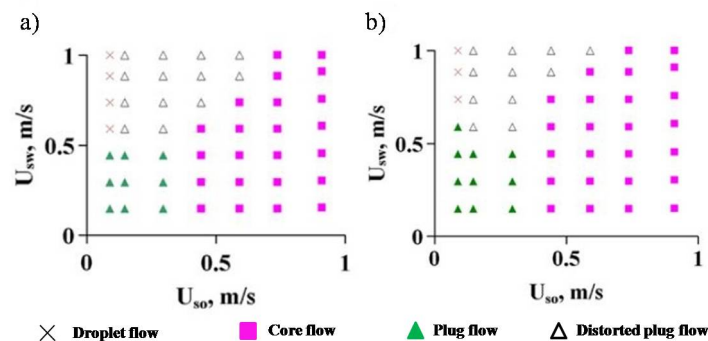


Figure 7-1: Flow pattern at different section and superficial velocity region, a) bend flow, b) return flow [9]

7-2 Geometry and boundary condition

In the figure 7-2 the geometry of 180° return bend is presented. The radius of the curved bend, R , is 0.10002 m and the radius of the tube, R_2 , is 0.006 m. The length of the straight pipe (at the inlet and outlet) is 0.06 m. The number of grid cells in the cross section is 3040, in the flow direction 103 grid cells are used. As mentioned the pipe lies in a horizontal plane, so the gravity force acts in a perpendicular direction to the pipe. The no-slip condition holds at the pipe wall. The initial velocity profile at the inlet was assumed to be given by the Li and Renardy [4] velocity profile. This initial profile was also assumed to be present in the internal flow region of the pipe at the start of the calculation.

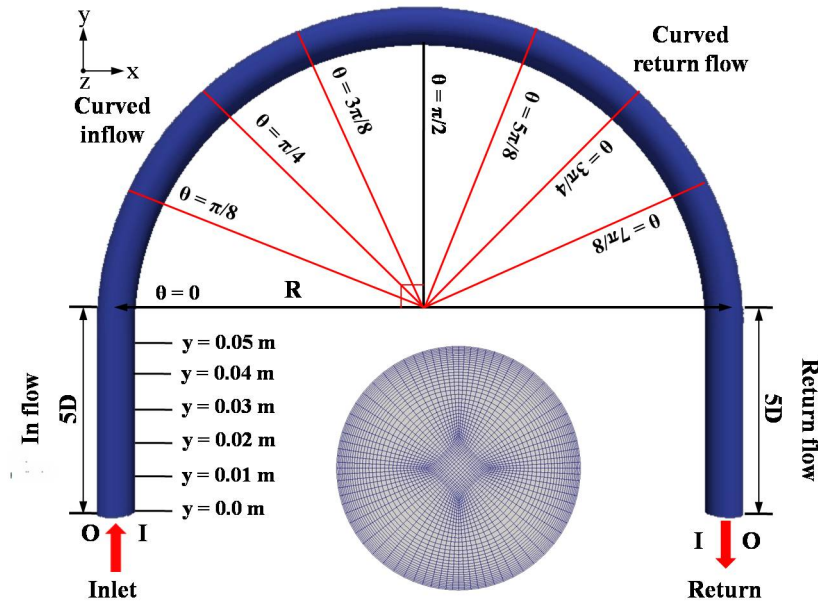


Figure 7-2: Geometry of 180° return bend

7-3 Parameter values

We applied the same fluid properties as used by Sharma et al. in their lubricating-oil experiments ($\rho_o = 960 \text{ kg/m}^3$, $\mu_o = 0.22 \text{ Pa} \cdot \text{s}$, $\sigma_o = 0.051 \text{ N/m}$) and water ($\rho_w = 999 \text{ kg/m}^3$, $\mu_w = 0.001 \text{ Pa} \cdot \text{s}$, $\sigma_w = 0.072 \text{ N/m}$).

In order to implement the initial core-annular flow profile of Li and Renardy into the flow the core diameter and pressure gradient were required. To calculate the core diameter we followed the empirical correlation proposed by Arney et al. [1993] for the straight pipe at the inlet. (This correlation was also used by Sharma et al [9]). According to this correlation the volume fraction of oil and water, V_o and V_w are given by

$$V_w = \beta[1 + 0.35(1 - \beta)] \quad (7-1)$$

$$V_o = 1 - V_w, \quad (7-2)$$

in which β is given by

$$\beta = \frac{Q_w}{Q_o + Q_w} = \frac{u_{s,w}^* \pi R_2^2}{u_{s,o}^* \pi R_2^2 + u_{s,w}^* \pi R_2^2} \quad (7-3)$$

where Q_o and Q_w are the volumetric flow rate of oil and water respectively. From equation 7-1, 7-2 and 7-3 we found that $\beta = 0.5$ and $V_w = 0.5875$. Using

$$V_w = \frac{A_w}{A} = 1 - \left(\frac{R_1}{R_2} \right)^2, \quad (7-4)$$

where A is cross section area of the pipe and A_w is the cross section area of the water flow, the core diameter can be calculated $R_1 = 0.003854$ m. Then the mixture Reynolds number with the mixture density, ρ_m , mixture viscosity, μ_m , and mixture velocity, U_m can be found from

$$Re_m = \frac{DU_m \rho_m}{\mu_m}, \quad (7-5)$$

in which

$$\rho_m = \rho_o \alpha_o + \rho_w (1 - \alpha_o) \quad (7-6)$$

and

$$\mu_m = 1 / \left(\frac{1 - \beta}{\mu_o} + \frac{\beta}{\mu_w} \right) \quad (7-7)$$

and

$$U_m = u_{s,w}^* + u_{s,o}^* \quad (7-8)$$

The following value was calculated $Re_m = 5897$.

From figure 7-3 of Sharma on next page the pressure gradient in the straight pipe at the inlet can be found. The result was $\Delta P/L = 1000$ Pa/m.

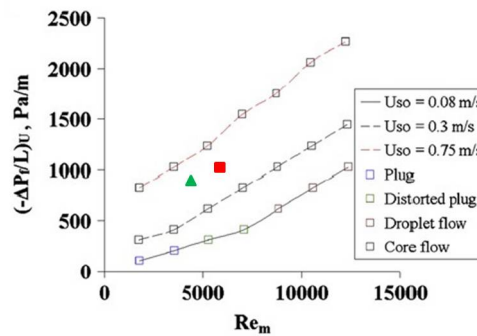


Figure 7-3: Pressure gradient as a function of mixture Reynolds number for the experiments by Sharma et al. The square with red color is the location of the mixture Reynolds number computed from the superficial oil velocities we selected, $u_{s,o}^* = 0.5$ m/s and $u_{s,w}^* = 0.5$ m/s. The green triangle is the location of recalculated mixture Reynolds number from the equation 3-4 and 3-5 to compare between Sharma, and Li and Renary [9]

As the core radius and pressure gradient at the inlet were now known we could calculate the initial velocity profile using the expression of Li and Renardy for a smooth core-annular flow. Also the superficial velocities for oil and water could be calculated. These superficial velocities were different (much larger) from the ones that we originally selected ($u_{s,o}^* = 0.5\text{m/s}$ and $u_{s,w}^* = 0.5\text{m/s}$). We considered the possible reasons for this discrepancy. Turbulence in the annular water layer was not likely the cause for the discrepancy, as the Reynolds number of the water flow was too low for turbulence to occur. Waves at the core-annular interface could be the reason, as in earlier studies we found that these waves have a significant influence on the pressure gradient. However, we did not study this possibility in more detail. In order to get superficial velocities that are closer to the originally chosen ones we adapted the pressure gradient in the Li and Renardy formula. For a pressure gradient of $\Delta P/L = 250\text{Pa/m}$ we found the following values for the superficial velocities $u_{s,w}^* = 0.3882\text{ m/s}$ and $u_{s,o}^* = 0.5462\text{ m/s}$. From these new superficial velocities we recalculated mixture Reynolds number and found $Re_m = 4595$. According to figure 7-3 we then found $\Delta P/L = 800\text{Pa/m}$, still much larger than the one used for the Li and Renardy velocity profile. We continued our calculation with $\Delta P/L = 250\text{Pa/m}$ and $R_1 = 0.003854\text{ m}$.

We realize that our comparison with the experimental data has become uncertain due to the mentioned difficulties. Again the reason could be the water turbulence or the waves at the core-annular interface. Using the velocity at the centerline of the core and the thickness of the annular layer we find for the Reynolds number in the annulus the value of $Re_2 = 1385$. It is not likely that this explains the discrepancy that we found.

7-4 Results

In our simulation we found fouling (the core touches the pipe wall) in the straight pipe at the pipe exit. Fouling is observed only after 0.6 seconds. In the straight pipe at the inlet and in the curved part of the pipe fouling is not observed at all time steps.

7-4-1 Core shape and position in the pipe

In the figure 7-4, 7-5 and 7-6 the shape and position of the core in the different parts of the return bend are presented. In the straight part at the inlet the flow remains a perfect core-annular flow at all times. The buoyancy effect is obviously not relevant in that part. In the curved part of the pipe the core moves to the outer-curved part of the pipe and starts deforming. It moves also slightly upwards due to the buoyancy effect. As mentioned fouling is not observed at the inlet and the curved part of the pipe. However in the straight pipe at the exit fouling is observed from time step 0.6 second. At the cross section at $y = 0.04$ and 0.05 fouling occurs, but disappears again. It is not clear, whether that will also take place at the other cross-sections and also further down the straight pipe at the exit. Figures 7-4, 7-5 and 7-6 are presented on the next page.

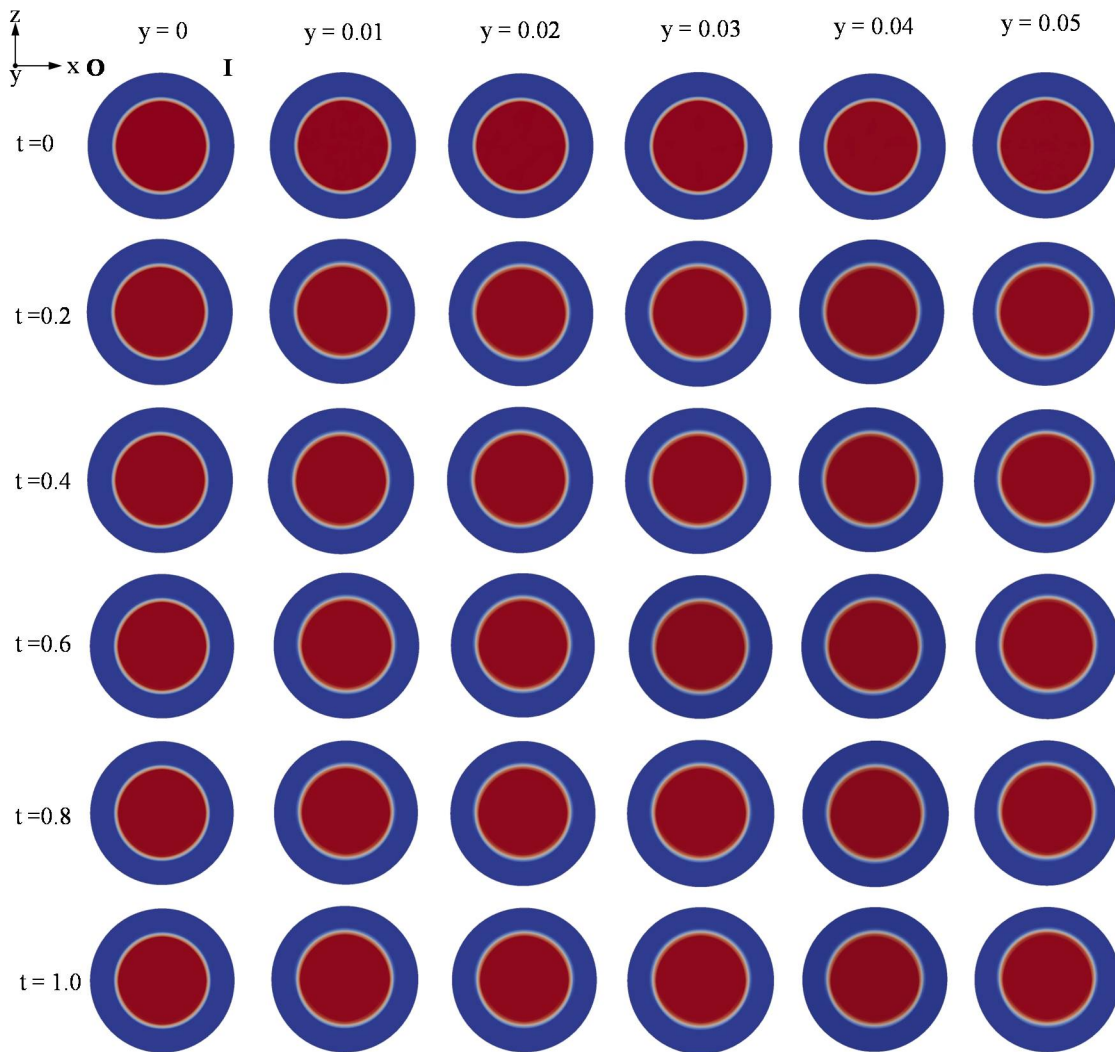


Figure 7-4: Core shape and position in the straight pipe at the inlet. The red and blue color indicate oil and water, respectively. $y = 0$ is at the inlet of the straight pipe. $y=0.5$ is at the transition of the straight pipe and the curved part of the pipe. (I: inner curve, O: outer curve)

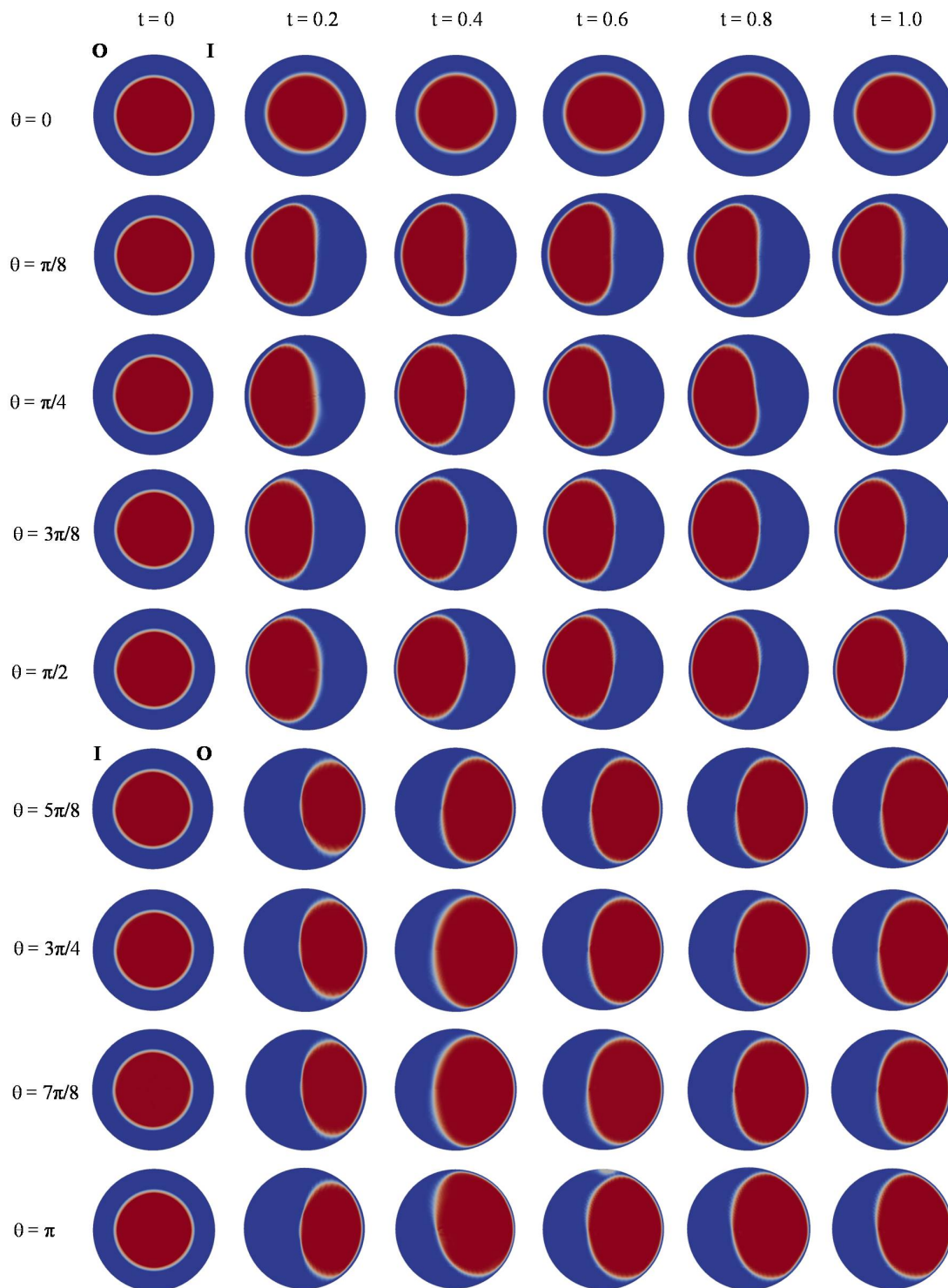


Figure 7-5: Core shape and position in the curved part of the pipe. The red and blue color indicate oil and water, respectively. $\theta = 0$ is at the inlet and $\theta = \pi$ is at the outlet of the curved part of the pipe. Return flow occurs from $\theta = 5\pi/8$ and the location of the inner and outer curve is opposite to that at the inflow (I: inner curve, O: outer curve)

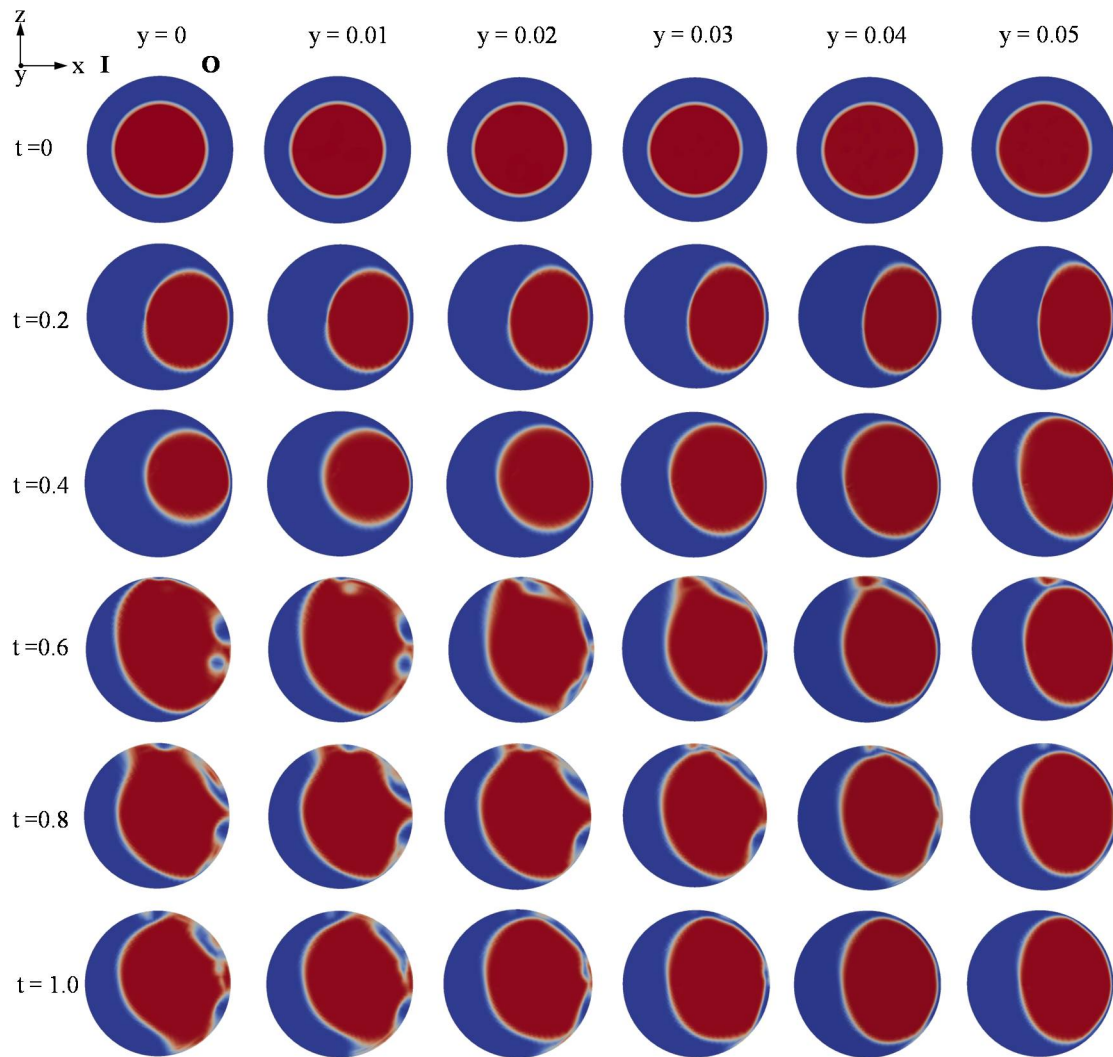


Figure 7-6: Core shape and position in the straight part of the pipe at the exit. The red and blue color indicate oil and water, respectively. $y = 0.5$ is at the transition between the curved part and the straight part of the pipe. $y = 0$ is exit of the straight part of the pipe. (I: inner curve, O: outer curve)

7-4-2 Secondary flows

In the straight pipe at the inlet no secondary flows occur. However in the curved part of the pipe secondary flows are present. In the figure 7-7 these secondary flows are shown. Enlarged versions of these figures are given in figure 7-15 and figure 7-16. As can be seen the vortices are stronger in the curved part of the pipe close to the inlet than in the part close to the exit. The strongest secondary flow is observed at $\theta = \pi/8$. Vortices are clearly visible at the $\theta = \pi/8, \pi/4$ and $3\pi/8$. This fact can be understood from the axial velocity profile. Compared to the curved part at the inlet the axial velocity in the curved part at the outlet is small. As a consequence the centrifugal force is also smaller and the vortices are weaker.

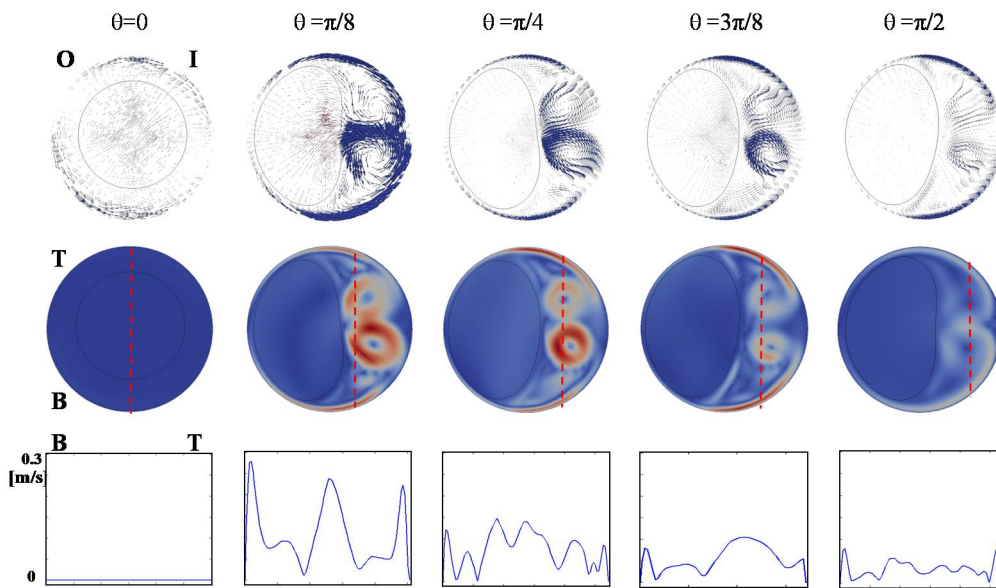


Figure 7-7: Secondary flow in the curved part of the pipe. (I: inner curve, O: outer curve, T: Top of the cross section, B: Bottom of the cross section)

7-4-3 Axial velocity

In the figure 7-8 the axial velocity profile in the straight part of the pipe at the inlet is given. No significant velocity change is observed. The core velocity is nearly constant due to the large viscosity compared to the water viscosity, and the water velocity decreases quickly from the interface between the core and the annulus to the wall.

In the curved part of the pipe the core moves to the outer-curve pipe wall and no longer remains constant. In the figure 7-9 and 7-10 the velocity profiles at the inlet part of the curved pipe and the outlet part are given respectively. At the $\theta = \pi/8$ and $\theta = \pi/4$ the axial velocity of annular is nearly constant except close to the interface and close to the pipe wall.

The maximum axial velocity in the straight pipe at the inlet is 1.326 m/s . In the curved

pipe the highest axial velocity is 1.292 m/s at the $\theta = 0$, inlet of curved pipe. The axial velocity in the straight pipe at the exit cannot be analysed due to the fouling.

The axial velocity distribution in a cross-section and its change is more clearly visible in the axial velocity contour map (see figure 7-11). Only the results for the curved part of the pipe are presented.

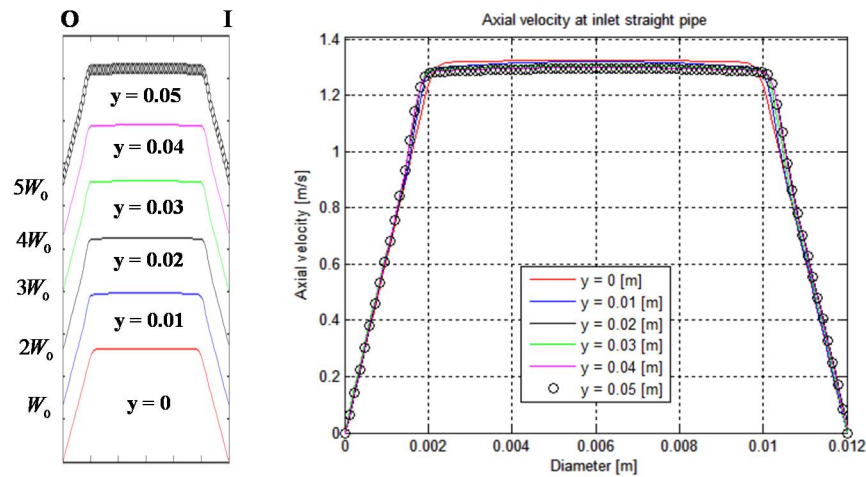


Figure 7-8: Axial velocity distribution in the straight pipe at the inlet. $y = 0$ is inlet of the inflow straight pipe. (I: inner curve, O: outer curve)

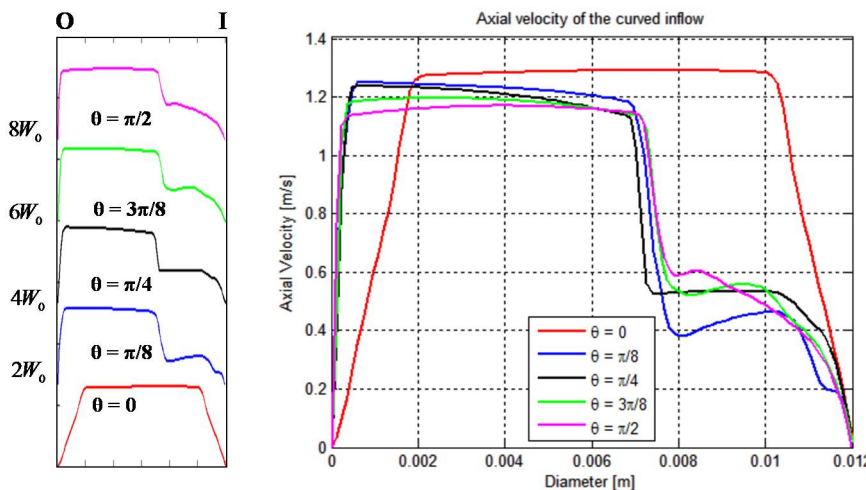


Figure 7-9: Axial velocity distribution in the curved inflow part of the pipe. $\theta = 0$ is inlet of the curved bend. (I: inner curve, O: outer curve)

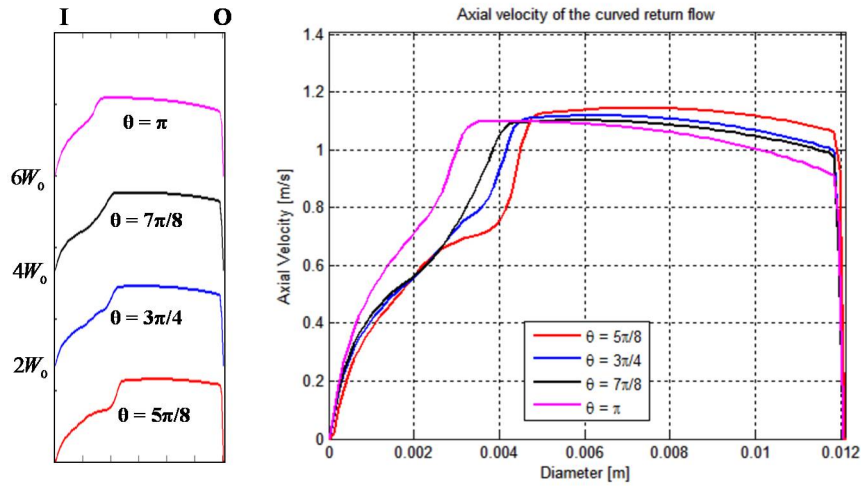


Figure 7-10: Axial velocity distribution in the curved return flow part of the pipe. $\theta = \pi$ is outlet of the curved return flow. For return flow the location of inner and outer curve is opposite compared to inflow (I: inner curve, O: outer curve)

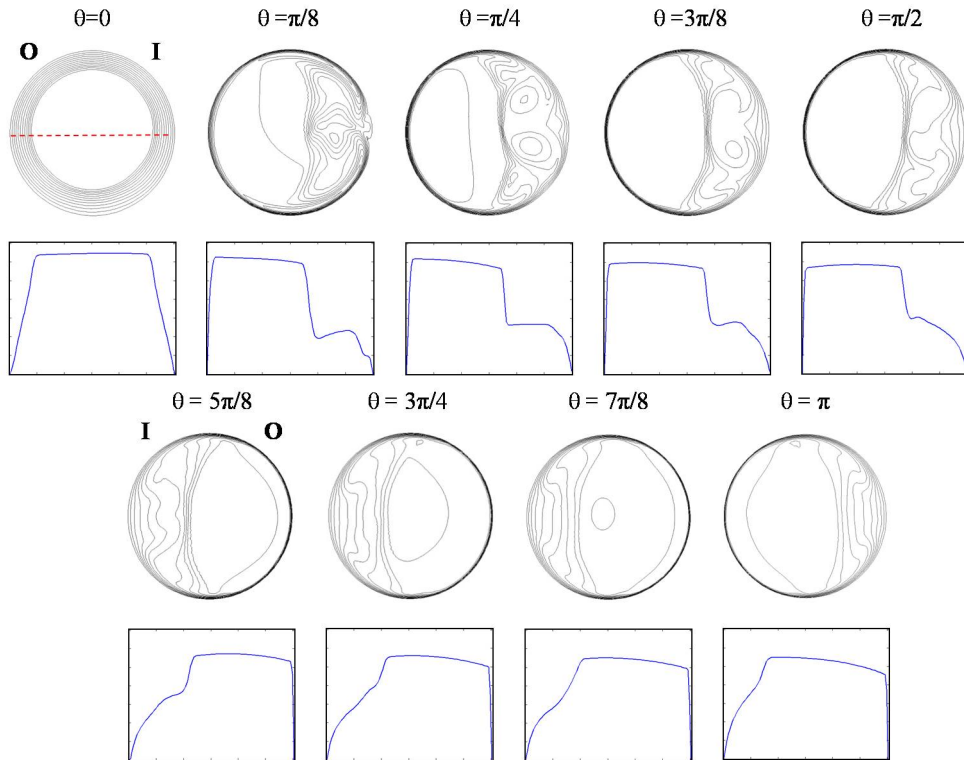


Figure 7-11: Axial velocity contour map in the curved part of the pipe, red dash is plot line. Return flow is from $\theta = 5\pi/8$ and the location of inner and outer curve is opposite compared to inflow (I: inner curve, O: outer curve)

7-4-4 Pressure distribution

In figure 7-12 the pressure distributions in the straight pipe at the inlet is given. The pressure distributions in the core are nearly constant except close to the curved part of the pipe. At $y=0.05$ m the centrifugal force effect has already started, and therefore the pressure distribution in the core is slightly tilted from the outer-curved part of the pipe to the inner-curved part. The pressure distribution in the curved-part of the pipe is given in figure 7-13. The left figure is for the part close to the inlet and the right figure for the part close to the outlet. As for the case of the 90° bend the pressure at the outer-curved part of the pipe increases, whereas it decreases at the inner-curved part. As can be seen the difference in pressure at the outer-curved part and the inner-curved part of the pipe is significantly lower out the outlet than at the inlet. Pressure contour maps for the curved part region of the the pipe are given in figure 7-14. Figures are presented in next page.

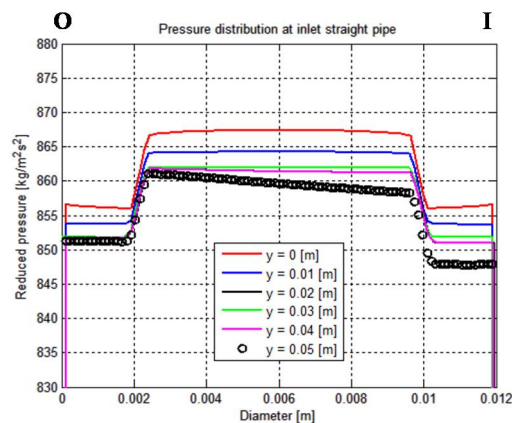


Figure 7-12: Pressure distribution in the straight pipe at the inlet. $y = 0$ is inlet of the inflow straight pipe. (I: inner curve, O: outer curve)

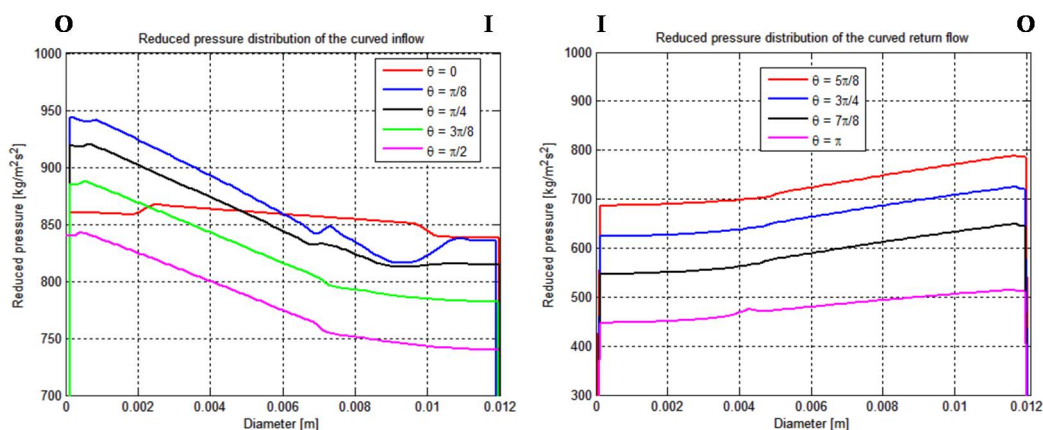


Figure 7-13: Pressure distribution in the curved part of the pipe. For return flow the location of inner and outer curve is opposite compared to inflow (I: inner curve, O: outer curve)

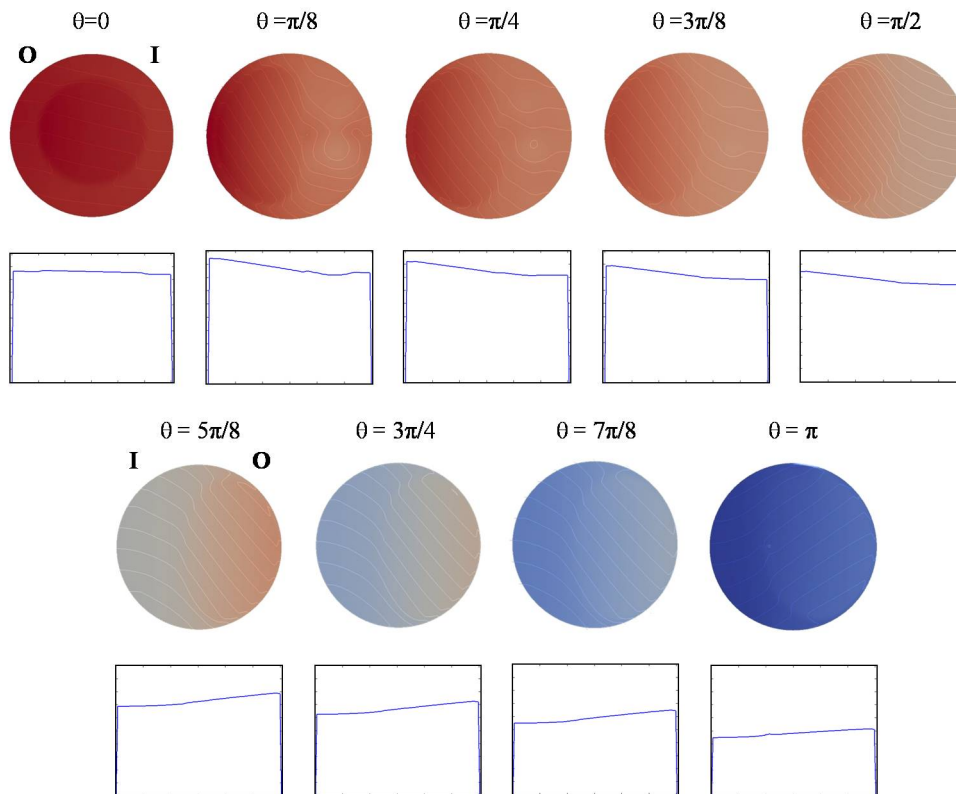


Figure 7-14: Pressure distribution contour map for the curved part of the pipe. Return flow is from $\theta = 5\pi/8$ and the location of inner and outer curve is opposite compared to inflow (I: inner curve, O: outer curve)

7-5 Conclusion

In this chapter we studied core-annular flow in 180° return bend. We paid attention to three parts of the return bend: the straight pipe at the inlet, the curved part of the pipe and the straight pipe at the outlet. In the curved part we found a secondary flow, that is almost symmetrical as the effect of the buoyancy force is small compared to the centrifugal force. In the curved part of the pipe the core moves to the outer-curved part of the pipe under the influence of the secondary flow. At the outlet we found a fouling of the pipe wall. We tried to compare our results with the experiments data of Sharma. However it turned out that the experimental initial pressure gradient and velocity profile could not be reproduced in our calculation. This is very likely due to the fact that in the experiments waves are present at the oil-water interface, whereas we assume a smooth interface.

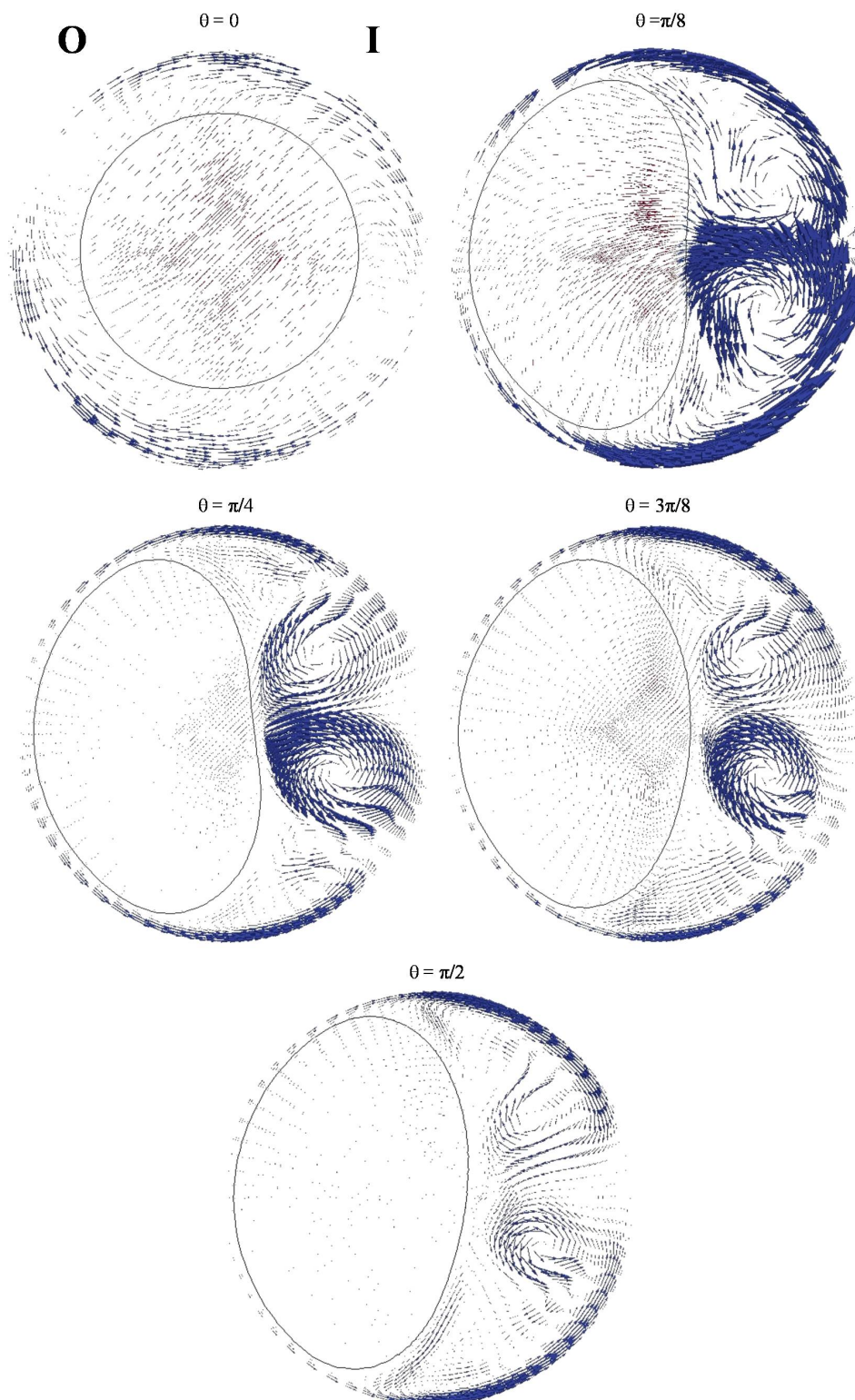


Figure 7-15: Secondary flow in the curved part of the pipe. The black circle line is interface between oil and water. (I: inner curve, O: outer curve)

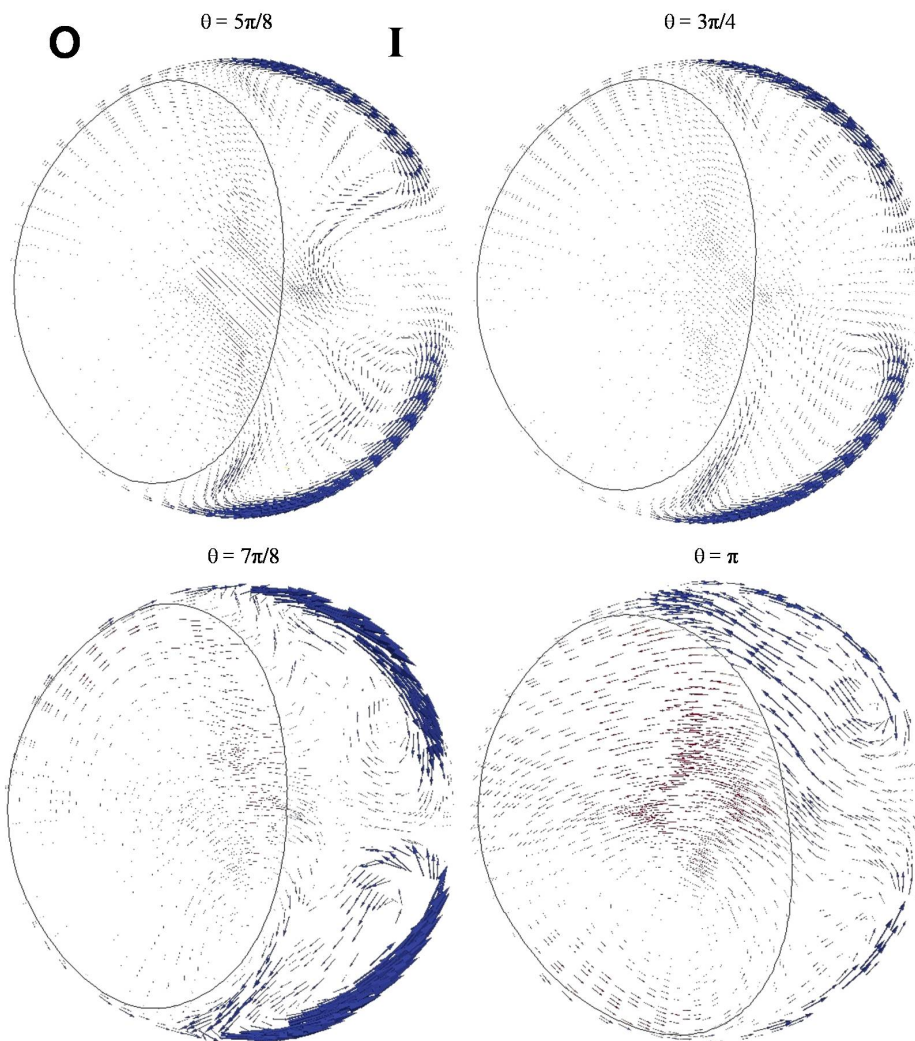


Figure 7-16: Secondary flow in the curved part of the pipe. The black circle line is interface between oil and water. For return flow the location of inner and outer curve is opposite compared to inflow (I: inner curve, O: outer curve)

Chapter 8

Recommendations

In this thesis we performed a numerical study of laminar core-annular flow. So not only the flow in the core is laminar, but also the flow in the annulus is supposed to be laminar. However in practice the annular flow can be turbulent. At the start of the project we tried to take the turbulence into account by using a RANS-model: the κ - ω model. (RANS model means Reynolds-averaged-Navier-Stokes model). We did not find reliable results. The problem of this model is that the calculation of the dissipation, specified by ω , is not accurate at the interface between high- and low-viscosity liquid. In order to solve this problem an additional damping term has to be added to ω equation. That requires a separate study.

In practise waves develop at the core-annular interface. These waves are essential for the counterbalancing of the buoyancy force on the core due to a density difference between the core liquid and annular liquid. In our study we have not paid attention to the wave development. A pipe of sufficient length is needed to see this development. However for a long pipe the computation time increases significantly. To avoid a too long computation time a possibility is to start already at the inlet with a wavy core-annular interface, but then also the initial velocity distribution needs to be adapted. This requires also a separate study.

A detailed study of grid refinement is also necessary. For our three-dimensional calculations this leads quickly to too large computation times. More study is needed for this numerical topic of three-dimensional core-annular flow.

Further research could also take place on real applications with different types of pipe. (Generally the studies about core-annular flow are focused on straight vertical or horizontal pipes.) Our study of core-annular flow can be considered as a first step in that direction. Also the influence of the temperature of the liquids on the physical parameters of the liquids (for instance the viscosity) needs further investigation.

Bibliography

- [1] G. Ooms, A. Segal, A. J. van der Wees, R. Meerhoff, and R. V. A. Oliemans "*A theoretical model for core-annular flow of a very viscous oil core and a water annulus through a horizontal pipe*" *Int. J. Multiphase Flow*, 10(1), 41 [1983]
- [2] D.D. Joseph, R. Bai, K. P. Chen, Y.Y. Renardy "*Core-Annular Flow*" *J. Fluid Mech*, 29:65-90 [1997]
- [3] V. R. Gopala and B. G. M. van Wachem "*Volume of fluid methods for immiscible fluid and free flows.*" *Chemical Engineering Journal* 141, pp. 204-221 [2008]
- [4] Li. J, Y.Y. Renardy "*Direct simulation of unsteady axisymmetric core-annular flow with high viscosity ratio*" *J. Fluid Mech*, 391:123-149 [1999]
- [5] R. Bai, K. Chen and Joseph. DD "*Lubricated pipelining: stability of core-annular flow. Part5. Experiments and comparison with theory*" *J. Fluid Mech*, VOL. 240, pp.97-132, 97-132 [1991]
- [6] G. Ooms, M. J. B. M. Pourquie, and J. C. Beerens "*On the levitation force in horizontal core-annular flow with a large viscosity ratio and small density ratio*" *Phys. Fluid* 25, 032102 [2013]
- [7] F. N. Van de Vosse "*A finite element analysis of the study laminar entrance flow in a 90° curved tube*" *International Journal for numerical methods in fluids*, VOL. 9, 275-287 [1989]
- [8] P. H. M. Bovendeerd, A. A. Van Steenhoven, F. N. Van de Vosse and G. Vossers, "*Steady entry flow in a curved pipe*" *J. Fluid Mech.*, 150, 139-158 [1987]
- [9] M. Sharma, P. Ravi, S. Ghosh, G. Das, O.K. Das "*Hydrodynamics of lube oil-water flow through 180° return bends*" *Chemical Engineering Science* 66 4468-4476 [2011]
- [10] D. D. Joseph, Y. Y. Renardy, "*Fundamentals of Two-Fluid Dynamics, Part II: Lubricated Transport, Drops and Miscible Liquids*" *Interdisciplinary Applied Mathematics*, VOL. 4 [1991]

- [11] V. Bertola *"Modeling and Experimentation in Two Phase Flow"* CISM courses and lectures No.450
- [12] J. C. Beerens *"Lubricated transport of heavy oil"* TU Delft, Master thesis
- [13] S. Ghosh, G. Das and P. K. Das *"Simulation of core annular in return bends-A comprehensive CFD study"* IChemE, 89: 2244-2253 [2011]
- [14] J. D. Issac and J. B. Speed *"Method of piping fluids"* US Patent No. 759374 [1904]
- [15] G. Ooms, M. J. B. M, Pourquie and P. Poesio *"Numerical study of eccentric -core annular flow"* Int. J. Multiphase Flow, VOL. 42, pp 74 [2012]
- [16] G. Ooms, Vuik and P. Poesio *"Core-annular flow through a horizontal pipe: Hydrodynamic counterbalancing of buoyancy force on core"* Physics of fluids 19, 092103 [2007]
- [17] J. R. Picardo and S. Pushpavanam *"Core-Annular Two-Phase Flow in a Gently Curved Circular Channel"* AIChE J, 59: 4871-4886 [2013]
- [18] W. Y. Soh and S. A. Berger *"Laminar entrance flow in a curved pipe"* J. Fluid Mech, VOL. 148, pp. 109-135 [1984]
- [19] H. Rusche *"Computational fluid dynamics of dispersed two-phase flows at high phase fraction"* Ph.D. dissertation, Imperial College of Science, Technology and Medicine [2000]
- [20] M. S. Arney, R. Bai, E. Guevara, D. D. Joseph, K. Liu *"Friction factor and hold up studies for lubricated pipelining-I. Experiments and correlations."* International Journal of Multiphase Flow 19, 1061-1067 [1993]
- [21] OpenFOAM *"www.openfoam.com"*